Research Square

Preprints are preliminary reports that have not undergone peer review.
They should not be considered conclusive, used to inform clinical practice,
or referenced by the media as validated information.

RNF19A couples tumour-intrinsic adaptation with immune suppression in castration-resistant prostate cancer and reveals sinomenine as a candidate intervention

Zhixuan Deng
the second affiliated hospital of University of South China
Huimei Liu
University of South China
Xi Sheng
the second affiliated hospital of University of South China
Mengyao Xie
the second affiliated hospital of University of South China
Yaohui He
Institute of Cell Biology of University of South China
Tao Jiang
the second affiliated hospital of University of South China
Pingyu Fu
the second affiliated hospital of University of South China
Xiangyang Zhang
the second affiliated hospital of University of South China
ZeYang Liao
First Affiliated Hospital of University of South China
Wanyan Xiong
Institute of Cell Biology of University of South China
Yixuan Deng
the second affiliated hospital of University of South China
Pengfei Lu
Institute of Cell Biology of University of South China
Ning Yang
yangning@usc.edu.cn

the second affiliated hospital of University of South China

Research Article

Keywords: RNF19A, castration-resistant prostate cancer, ubiquitination, p53, RELA, tumour metabolism, tumour immunity, sinomenine

Posted Date: November 11th, 2026

DOI: https://doi.org/10.21203/rs.3.rs-11507047/v1

License: This work is licensed under a Creative Commons Attribution 4.0 International License.
Read Full License

Additional Declarations: No competing interests reported.

RNF19A couples tumour-intrinsic adaptation with immune suppression in castration-resistant prostate cancer and reveals sinomenine as a candidate intervention

[1,2,3]ZhiXuan Deng[†], [1,3,4]HuiMei Liu[†], [1,2]Sheng Xi, [1,2]Mengyao Xie，[2]Yaohui He,[1]Tao Jiang,[1]Pingyu Fu，[1]Xiangyang Zhang, [5]ZeYang Liao，[3]Wanyan Xiong, [1,2]Yixuan Deng, [2,3]Pengfei Lu[*], [1,2] Ning Yang[*]

[1]The Second Affiliated Hospital, Hengyang Medical School, University of South China, Hengyang, Hunan 421000, China

[2] Institute of Cell Biology, Hengyang Medical School, University of South China, Hengyang, Hunan 421000, China

[3] The Affiliated Nanhua Hospital, University of South China, Hengyang, Hunan, China

[4] College of Basic Medical Science, Hengyang Medical School, University of South China, Hengyang, 421001, China.

[5]The First Affiliated Hospital, Hengyang Medical School, University of South China, Hengyang, Hunan 421001, China

*Address correspondence to:

Ning Yang, yangning@usc.edu.cn

Keywords: RNF19A; castration-resistant prostate cancer; ubiquitination; p53; RELA; tumour metabolism; tumour immunity; sinomenine

Running Title: RNF19A links CRPC adaptation and immune suppression

Number of Figures: 7

ABSTRACT

Castration-resistant prostate cancer (CRPC) is characterized by tumour-cell adaptation and an immunosuppressive microenvironment, yet the molecular regulators linking these processes remain incompletely defined. By integrating single-cell transcriptomic datasets from hormone-sensitive prostate cancer and CRPC, we identified the E3 ubiquitin ligase ring finger protein 19A (RNF19A) as a CRPC-associated regulator enriched in basal-like epithelial cells. RNF19A depletion impaired prostate-cancer cell growth and tumour formation, increased apoptosis, and suppressed metabolic programmes related to ATP production and oxidative phosphorylation. Unbiased immunoprecipitation–mass spectrometry identified p53 as an RNF19A-interacting protein, and subsequent analyses showed that RNF19A promoted p53 ubiquitination and proteasome-dependent degradation, thereby supporting tumour-cell survival. RNF19A depletion also induced NF-κB- and inflammation-associated transcriptional programmes, suggesting that RNF19A may influence the inflammatory and immune-regulatory state of the tumour microenvironment. Spatial transcriptomic analysis showed that RNF19A-high tumour-like niches were associated with suppressive myeloid and exhausted-CD8-like programmes. Consistent with this observation, RELA was also identified as an RNF19A-interacting protein, and RNF19A promoted RELA ubiquitination and degradation, thereby restraining RELA-dependent NF-κB signalling, chemokine production and antigen-presentation-related programmes. Finally, structure-guided natural-product screening identified sinomenine as a candidate RNF19A-binding compound. Sinomenine bound recombinant RNF19A, reduced RNF19A abundance, inhibited prostate-cancer cell and patient-derived organoid growth, and suppressed xenograft growth. Together, these findings show that RNF19A sustains CRPC progression by promoting p53 and RELA degradation, thereby enhancing tumour-cell survival while limiting inflammatory and antigen-presentation-associated signalling. RNF19A therefore represents a potential therapeutic target in CRPC.

INTRODUCTION

Prostate cancer is among the most commonly diagnosed malignancies and remains a leading cause of cancer-related death in men worldwide[1]. Androgen-deprivation therapy is the cornerstone of systemic treatment for advanced prostate cancer, and the addition of more potent androgen receptor (AR) pathway inhibitors, including abiraterone and enzalutamide, have substantially prolonged survival[2,3]. Nevertheless, treatment responses are rarely durable, and most patients with advanced disease eventually develop castration-resistant prostate cancer (CRPC). CRPC is not driven solely by restoration of canonical AR signalling but encompasses heterogeneous adaptive programmes involving AR reprogramming, lineage plasticity, stress tolerance, metabolic rewiring and treatment resistance[4]. Understanding how prostate cancer cells survive sustained therapeutic pressure and maintain castration resistance therefore remains a major challenge.

CRPC is not defined by a single molecular phenotype. Although many tumours retain AR activity, prolonged androgen deprivation or AR-pathway inhibition can select for tumour-cell states that extend beyond the conventional AR-high luminal identity. Alterations in TP53 and RB1, for example, promote lineage plasticity, mixed-lineage differentiation and antiandrogen resistance[5,6]. In parallel, inflammatory signalling, including JAK/STAT activity, has been implicated in the emergence of AR-independent and treatment-tolerant states[7]. Single-cell studies have further revealed progenitor-like, mixed-lineage and other treatment-associated epithelial programmes in advanced prostate cancer[7-9]. These observations indicate that CRPC progression involves dynamic remodelling of tumour-cell states rather than the simple expansion of a pre-existing AR-dependent population.

Metabolic adaptation is another important component of this process. Hormone-sensitive prostate cancer (HSPC) and CRPC display distinct metabolic profiles, and treatment-resistant prostate-cancer cells can reprogramme mitochondrial metabolism, oxidative phosphorylation and fatty-acid utilization to maintain bioenergetic fitness under therapeutic stress[10,11]. At the same time, CRPC is frequently associated with an immunosuppressive tumour microenvironment and limited responsiveness to immune-checkpoint blockade[10]. Impaired interferon and chemotactic signalling, accumulation of suppressive myeloid populations and reduced infiltration or dysfunction of cytotoxic T cells have all been linked to treatment resistance[8,9,11]. Importantly, tumour-cell adaptation and immune remodelling are unlikely to represent independent processes. Changes in

tumour-cell state, metabolism and protein secretion can alter antigen presentation, chemokine production and immune-cell engagement, whereas immune-derived signals can in turn shape tumour-cell survival and phenotypic plasticity. However, the molecular regulators that coordinate tumour-cell fitness with tumour-derived immune signals in CRPC remain poorly defined.

Post-translational regulation by the ubiquitin-proteasome system provides a plausible mechanism for integrating these diverse features of tumour adaptation. E3 ubiquitin ligases determine substrate specificity within ubiquitin-dependent protein turnover and can consequently control multiple biological outputs from a single tumour-cell state. By regulating the stability of transcription factors, signalling components and metabolic regulators, an E3 ligase may simultaneously influence tumour-cell survival, cellular energetics and communication with the immune microenvironment[12,13]. This substrate-specific mode of regulation is particularly relevant in CRPC, where treatment resistance depends on the coordinated activity of several adaptive programmes rather than on one isolated pathway. Nevertheless, the E3 ligases that connect CRPC-associated epithelial states to metabolic and immune remodelling remain incompletely characterized.

Ring finger protein 19A **(**RNF19A) is an RBR-type E3 ubiquitin ligase that has previously been associated with aggressive prostate-cancer features and with regulatory pathways linked to castration resistance[14]. RNF19A has also been implicated in the post-translational regulation of proteins involved in genome maintenance and antiviral signalling[15], suggesting that it may influence tumour behaviour through context-dependent substrate selection. Whether RNF19A contributes to the maintenance of CRPC-associated tumour-cell states, and whether it coordinates tumour-intrinsic adaptation with tumour-immune communication, has not been established. In particular, it remains unclear whether RNF19A controls the stability of key tumour-suppressive or inflammatory signalling proteins in prostate-cancer cells.

Here, we integrated single-cell transcriptomic and intercellular-communication analyses of HSPC and CRPC to identify epithelial regulators associated with the altered tumour ecosystem. This analysis nominated RNF19A as a CRPC-associated E3 ubiquitin ligase enriched in basal-like epithelial states. Using genetic perturbation in prostate-cancer models, we show that RNF19A supports tumour-cell growth, survival, mitochondrial activity and oxidative metabolism. Mechanistically, RNF19A interacts with p53 and promotes its ubiquitination and proteasome-

associated turnover, providing a potential basis for its tumour-cell-intrinsic effects. We further demonstrate that RNF19A interacts with RELA/p65 and limits NF-κB-dependent chemokine, antigen-presentation and immune-interaction programmes in tumour cells. RNF19A depletion consequently alters CD8 T-cell-associated phenotypes in spatial and co-culture models. Finally, structure-guided screening and biochemical binding analyses identify sinomenine (SIN) as a candidate RNF19A-binding compound that reproduces several phenotypes associated with RNF19A depletion in cellular, organoid and xenograft models. Together, these findings define RNF19A as a substrate-dependent proteostatic regulator that links CRPC-associated tumour-cell fitness to tumour-derived immune signalling and provide a chemical starting point for investigating RNF19A-directed therapeutic strategies.

RESULTS

Integrated single-cell analysis identifies RNF19A as a CRPC-associated E3 ubiquitin ligase

We first asked whether progression from hormone-sensitive prostate cancer (HSPC) to CRPC was accompanied by a broader reorganization of the tumour ecosystem. This question was important because a candidate tumour regulator could emerge from altered interactions between epithelial, stromal and immune compartments, rather than from one isolated cell population. To address this question, we integrated public single-cell RNA-sequencing datasets from HSPC and CRPC. The count-matched atlas contained 12 HSPC and 12 CRPC samples and comprised 78,758 cells. Unsupervised clustering and transferred cell-type annotations were evaluated using canonical lineage markers before disease-state comparisons were performed **(Fig. 1A-C; Supplementary Fig. 1A-C)**.

The integrated representation resolved nine major cellular compartments: basal, luminal and neuroendocrine epithelial cells, together with T cells, B cells, myeloid cells, mast cells, stromal cells and endothelial cells. HSPC- and CRPC-derived cells occupied overlapping regions of the embedding, indicating that the two disease states retained the same major cell classes. Their relative distributions nevertheless differed across several regions of the map **(Fig. 1B-C)**. These findings suggested that CRPC progression involved changes in the abundance or state of shared populations, rather than the simple appearance of an entirely new cellular compartment.

We then compared predicted intercellular communication using CellChat. The global number of inferred interactions increased from 833 in HSPC to 1,156 in CRPC, whereas the displayed aggregate interaction strength increased from approximately 0.001 to 0.003 **(Fig. 1D-F; Supplementary Fig. 1D-G)**. Incoming and outgoing signalling profiles also changed across multiple cell classes, including basal-like epithelial cells. Thus, CRPC was associated with a denser and differently organized predicted communication network. This result provided the rationale for focusing on basal-like epithelial cells and searching for tumour-intrinsic regulators linked to the altered CRPC ecosystem.

Because basal-like epithelial cells changed their predicted sender and receiver roles in CRPC, we next asked whether this compartment contained a tractable disease-associated regulator. We focused on E3 ubiquitin ligases because they can coordinate protein turnover and thereby connect a tumour-cell state with several downstream programmes. We performed a sample-level pseudobulk comparison of basal-like cells from all eligible samples containing this population. The edgeR quasi-likelihood analysis used the displayed thresholds of a false-discovery rate below 0.05 and an absolute log2 fold change of at least 1 **(Fig. 1G)**.

The resulting CRPC-associated gene set was intersected with three additional candidate sets: annotated E3 ubiquitin ligases, survival-associated genes and relatively unexplored genes. RNF19A was located in the four-way intersection and was therefore selected for experimental follow-up **(Fig. 1H)**. In the independent cell-level display, RNF19A expression distributions differed between HSPC and CRPC basal-like cells ($P = 8.60 \times 10^{-10}$; **Supplementary Fig. 1H**). This comparison was treated as descriptive support rather than patient-level inference.

We then asked whether RNF19A carried clinical information. In the displayed survival analysis, the RNF19A-high group had a poorer outcome than the RNF19A-low group. The hazard ratio was 1.80 (95% confidence interval, 1.24-2.61), and the log-rank P value was 0.0017 **(Fig. 1I)**. Together, the altered communication landscape, basal-cell pseudobulk screen, four-way candidate intersection and survival association nominated RNF19A as a CRPC-associated E3 ubiquitin ligase. This integrated evidence established RNF19A as a candidate that could plausibly connect tumour-cell state, protein turnover and progression-related phenotypes.

RNF19A promotes prostate-cancer cell growth and suppresses apoptosis

We next asked whether RNF19A was expressed in experimental prostate-cancer models and whether its depletion affected tumour-cell growth. Establishing both points was necessary before investigating a molecular mechanism. RNF19A messenger RNA and protein were compared among RWPE-1 prostate epithelial cells and the LNCaP and DU145 prostate-cancer cell lines. RNF19A protein was visibly more abundant in both cancer cell lines than in RWPE-1 cells **(Fig. 2A; Supplementary Fig. 2A-B)**. This comparison supported the use of LNCaP and DU145 as two independent cellular contexts for loss-of-function experiments.

Three RNF19A-targeting siRNAs were screened by RT-qPCR and Western blot. All three reduced RNF19A to different degrees, and si-RNF19A#1 produced the strongest displayed knockdown in both cell lines **(Supplementary Fig. 2C-H)**. We therefore used the most effective sequence for the downstream transient-knockdown assays. This initial validation also reduced the likelihood that subsequent phenotypes would be interpreted from an insufficiently effective perturbation.

RNF19A depletion reduced several complementary growth-related readouts. CCK-8 signal accumulated more slowly over the 0-96 h time course in both cell lines **(Supplementary Fig. 2I)**. Colony-formation efficiency fell to approximately 30% of control in LNCaP cells and 40% in DU145 cells **(Fig. 2B; Supplementary Fig. 2J)**. RNF19A-depleted cultures also formed fewer spheres than the matched siRNA controls **(Fig. 2C-D)**. Together, these results showed that RNF19A depletion reduced short-term growth, clonogenic capacity and sphere formation.

Because reduced colony formation and CCK-8 signal could partly reflect increased cell death, we next assessed apoptosis. We evaluated this question using flow cytometry, apoptosis-associated proteins and DNA-fragmentation assays. Annexin V-FITC/propidium iodide flow cytometry showed a marked shift towards Annexin V-positive quadrants after RNF19A silencing **(Fig. 2E-F)**. In the representative LNCaP profiles, the two right-hand quadrants increased from a combined 1.24% in si-NC cells to 11.69% after RNF19A knockdown. The corresponding values increased from 4.03% to 19.78% in DU145 cells. The group summaries showed the same direction in both cell lines.

Western blot provided an independent protein-level readout. RNF19A depletion reduced Bcl2 and the displayed pro-caspase-3 signal while increasing the cleaved-caspase-3 signal **(Fig. 2G-H; Supplementary Fig. 2K-L)**. TUNEL microscopy also showed more DNA-fragmentation-positive cells after RNF19A depletion in both LNCaP and DU145 cultures **(Fig. 2I-J)**. The agreement

among Annexin V staining, apoptosis-associated protein changes and TUNEL positivity indicated that increased apoptosis contributed to the growth phenotype caused by RNF19A loss.

Transient siRNA experiments established an acute phenotype, but they did not determine whether RNF19A was required during prolonged growth. We therefore generated stable shRNA-mediated RNF19A-knockdown models and tested them in long-term culture and subcutaneous tumours. Stable RNF19A knockdown reduced RNF19A messenger RNA in both LNCaP and DU145 cells **(Supplementary Fig. 3A).** Colony-formation assays and the 0-96 h CCK-8 time course remained lower in shRNF19A cultures than in sh-control cultures **(Supplementary Fig. 3B-D)**. These observations reproduced the transient-knockdown phenotype using a second perturbation format.

We then implanted control or RNF19A-depleted tumour cells subcutaneously. Three tumours per group were displayed in the final figure set **(Fig. 2K-L; Supplementary Fig. 3E)**. Tumour dimensions were recorded on days 10, 13, 16, 19 and 22. The shRNF19A group followed a lower volume trajectory and had a lower terminal tumour-weight readout than the sh-scramble group **(Fig. 2M-N)**. Histological and fluorescence analyses asked whether the in vivo growth difference was accompanied by changes within the excised tumours. The displayed histology-derived compactness metric was lower after RNF19A knockdown **(Fig. 2O-P)**. RNF19A fluorescence decreased, confirming maintenance of the perturbation, whereas tumour TUNEL positivity increased **(Fig. 2Q-S; Supplementary Fig. 3F)**.

Thus, RNF19A loss produced concordant short-term, long-term and in vivo phenotypes. Decreased clonogenic and sphere-forming capacity was accompanied by increased apoptosis in two prostate-cancer cell lines. The lower tumour burden and higher TUNEL signal extended these observations to the displayed subcutaneous model. Collectively, these results established RNF19A as a positive regulator of prostate-cancer growth and survival, and provided a functional basis for examining the pathways through which RNF19A supports tumour-cell fitness.

RNF19A sustains metabolic programmes and mitochondrial activity

To explore the biological programmes associated with RNF19A expression, we stratified basal-like epithelial cells into RNF19A-high and RNF19A-low groups using the single-cell transcriptomic data and performed differential-expression and pathway-enrichment analyses. Genes enriched in RNF19A-high cells were associated with several biological processes, including cell adhesion, migration and MAPK signalling. Immune-associated pathways, including cytokine-

receptor interactions, chemokine signalling and T-cell-receptor-related signalling, were also represented. In parallel, the enrichment results included metabolic processes related to lipid localization, fatty-acid transport, ether-lipid metabolism and arachidonic-acid metabolism **(Fig. 3A-B; Supplementary Fig. 4A-B)**. These single-cell associations suggested that high RNF19A expression accompanied coordinated alterations in immune-related signalling and cellular metabolism.

We next performed bulk RNA sequencing to determine the transcriptional consequences of RNF19A depletion. The analysis used three independently cultured shScr samples and three independently cultured shRNF19A samples. RNF19A knockdown induced broad transcriptional changes, with both upregulated and downregulated genes observed in the differential-expression analysis. Genes with the largest expression changes clearly distinguished shRNF19A from control samples in the heatmap **(Fig. 3C-D)**.

Functional enrichment analysis revealed a prominent reduction in metabolic programmes following RNF19A knockdown. Genes decreased after RNF19A depletion were enriched for ATP biosynthesis, aerobic respiration and oxidative phosphorylation, together with fatty-acid metabolism and fatty-acid elongation pathways **(Fig. 3E-F)**. In contrast, genes increased after RNF19A knockdown were associated with several immune- and inflammatory-related processes, including TNF and NF-κB signalling, cytokine-receptor signalling, leukocyte migration and regulation of phagocytosis **(Fig. 3E-F; Supplementary Fig. 5A-B)**. Thus, the perturbation produced two linked transcriptional features: suppression of energy-metabolism programmes and release of inflammatory signalling programmes.

Because several metabolic pathways decreased after RNF19A knockdown, we asked whether these transcriptional changes were accompanied by functional alterations in cellular energy metabolism. We combined ranked gene-set analysis, extracellular-flux measurements, ATP-production-rate measurements and mitochondrial imaging. Gene-set enrichment analysis showed significant depletion of all four prespecified metabolic programmes after RNF19A knockdown. Gene-set enrichment analysis showed significant depletion of glycolysis, mitochondrial respiration, mTORC1 signalling and oxidative phosphorylation after RNF19A knockdown, with mitochondrial respiration showing the strongest negative enrichment (**Fig. 3G**). These results showed that the pathway-level effects were not limited to one branch of metabolism.

We next monitored oxygen-consumption rate (OCR) and extracellular-acidification rate (ECAR) in LNCaP and DU145 cells. RNF19A knockdown lowered the baseline OCR and ECAR profiles in both cell lines. The control and knockdown groups also followed different trajectories after sequential oligomycin and rotenone/antimycin A injection **(Fig. 3H)**. Consistent with these flux profiles, calculated mitochondrial ATP and glycolytic ATP production rates were reduced after RNF19A depletion **(Fig. 3I)**. The simultaneous reduction of both ATP-producing components indicated that the cells did not fully compensate for impaired mitochondrial activity by increasing glycolytic ATP production.

MitoTracker Orange imaging provided an orthogonal cellular readout. WGA outlined the cell surface, Hoechst marked nuclei and MitoTracker Orange reported active mitochondrial signal **(Fig. 3J)**. Relative MitoTracker fluorescence decreased after RNF19A knockdown in both LNCaP and DU145 cells **(Fig. 3K)**. The agreement among bulk transcriptional profiling, four significant GSEA results, extracellular-flux measurements, ATP-production-rate estimates and mitochondrial imaging supported a common conclusion. RNF19A was required to maintain metabolic gene programmes, cellular bioenergetic output and active-mitochondrial fluorescence in the tested prostate-cancer models.

These data also provided a bridge to the next mechanistic analyses. The metabolic phenotype occurred together with increased apoptosis after RNF19A loss, suggesting that an RNF19A-regulated protein could coordinate survival and energy metabolism. At the same time, the induction of inflammatory programmes suggested that a second substrate might connect RNF19A to tumour-immune signalling. We therefore used an unbiased protein-interaction screen to identify candidate proteins that could explain these two branches of the phenotype.

RNF19A binds p53 and promotes its proteasome-associated turnover

To identify proteins that might mediate the biological effects of RNF19A, we performed an unbiased interaction screen using anti-FLAG affinity purification followed by mass spectrometry in cells expressing FLAG-tagged RNF19A. Comparison with the control immunoprecipitation identified proteins preferentially associated with RNF19A, among which p53 emerged as a candidate for further investigation **(Fig. 4A-B)**. p53 was of particular interest because attenuation of its tumour-suppressive activity is a recurrent feature of advanced prostate cancer. In addition to its canonical roles in cell-cycle control and apoptosis, p53 participates in the regulation of mitochondrial respiration, oxidative phosphorylation and glycolytic homeostasis. It therefore

represented a plausible molecular link between the survival and metabolic phenotypes observed after RNF19A depletion.

We first examined p53 abundance across prostate epithelial and cancer-cell models. Compared with non-malignant RWPE-1 cells, the displayed p53 protein abundance was lower in LNCaP and DU145 prostate-cancer cells **(Supplementary Fig. 6A-B)**. Together with the higher RNF19A abundance observed in the cancer-cell models, this inverse pattern raised the possibility that RNF19A contributed to reduced p53 protein abundance. We therefore asked whether RNF19A physically associated with p53 and whether altering RNF19A expression changed p53 stability.

Reciprocal co-immunoprecipitation confirmed that RNF19A and p53 were present in the same protein complex. Immunoprecipitation of RNF19A recovered endogenous p53, whereas reciprocal immunoprecipitation of p53 recovered RNF19A. Matched IgG controls showed no comparable co-precipitation **(Fig. 4C)**. Confocal microscopy further showed substantial cellular colocalization of RNF19A and p53 **(Fig. 4D)**. These experiments established cellular association using two independent approaches.

We next asked whether the interaction could occur directly. In a recombinant protein pull-down assay, purified GST-RNF19A retained His-p53, whereas GST alone did not show comparable retention **(Fig. 4E)**. The recombinant result, together with reciprocal co-immunoprecipitation and cellular colocalization, supported a direct physical interaction between RNF19A and p53. Because these assays did not map the binding interface, subsequent experiments focused on the functional consequence of the interaction rather than assigning a specific contact site.

RNF19A knockdown markedly increased p53 protein abundance in LNCaP cells, whereas re-expression of an RNAi-resistant RNF19A construct reversed this increase and restored p53 towards the control level **(Fig. 4F-G; Supplementary Fig. 6D)**. The same knockdown-rescue relationship was reproduced in DU145 cells **(Supplementary Fig. 6E-F)**. In contrast to the clear change at the protein level, TP53 messenger RNA abundance was not detectably altered after RNF19A depletion (**Fig. 4H**). The separation between protein and transcript responses indicated that RNF19A regulated p53 predominantly at the post-transcriptional level.

Because RNF19A is an E3 ubiquitin ligase, we next tested whether the reduction in p53 protein involved protein degradation. Pharmacological inhibition showed that blockade of the proteasome with MG132 prevented RNF19A-associated p53 loss more effectively than inhibition

of the lysosomal pathway with chloroquine **(Fig. 4I-J; Supplementary Fig. 6G-H)**. This result implicated the ubiquitin-proteasome system as the major pathway responsible for RNF19A-dependent regulation of p53 abundance.

Consistent with this interpretation, p53 immunoprecipitation followed by ubiquitin Western blot showed that RNF19A depletion substantially reduced the p53-associated ubiquitin smear. Re-expression of RNAi-resistant RNF19A restored p53-associated ubiquitination **(Fig. 4K-L)**. Thus, RNF19A expression was required for efficient p53 ubiquitination under these conditions. These experiments did not determine the ubiquitin-chain linkage or demonstrate ubiquitin transfer in a fully reconstituted cell-free system. They nevertheless placed p53 ubiquitination downstream of RNF19A expression and upstream of the observed change in protein abundance.

Finally, we directly assessed p53 turnover using cycloheximide-chase assays. Following inhibition of new protein synthesis, p53 progressively declined in control cells, whereas its decay was delayed after RNF19A knockdown **(Fig. 4M-N)**. Thus, depletion of RNF19A prolonged p53 protein stability, consistent with the proteasome-inhibition and ubiquitination experiments. The concordance among knockdown-rescue, transcript-protein separation, degradation-pathway inhibition, ubiquitination and half-life measurements supported a coherent mechanism.

Together, these results identified p53 as an RNF19A-interacting protein and showed that RNF19A promoted its ubiquitination and proteasome-associated turnover in prostate-cancer cells. Given the functions of p53 in apoptosis and cellular energy metabolism, RNF19A-mediated p53 destabilization provided a mechanistic framework connecting elevated RNF19A with both the survival advantage and metabolic adaptation observed in the preceding experiments. This mechanism explained the tumour-cell-intrinsic branch of the RNF19A phenotype, but it did not by itself account for the immune-related transcriptional changes induced by RNF19A depletion.

RNF19A-high tumour regions are associated with suppressive immune programmes

Our transcriptomic analyses suggested that the effects of RNF19A were not restricted to tumour-cell-intrinsic growth and metabolism. In the single-cell analysis, RNF19A-high basal-like epithelial cells were associated with cytokine-, chemokine- and other immune-related signalling programmes. In the perturbation analysis, RNF19A depletion increased TNF-, NF-κB- and inflammatory-related transcriptional programmes. These observations raised the possibility that RNF19A might also influence tumour-immune communication. We therefore asked whether RNF19A-high tumour regions in CRPC were associated with a distinct immune microenvironment.

To address this question in spatial context, we analysed a quality-controlled spatial transcriptomic section from CRPC tissue and annotated tumour-like, stromal-rich, immune-enriched and mixed regions **(Fig. 5A-B; Supplementary Fig. 7A-G)**. RNF19A expression was heterogeneous across the tissue section. We therefore identified tumour-like spots and stratified them as RNF19A-high, RNF19A-medium or RNF19A-low for spatial-neighbourhood analyses **(Fig. 5C)**. This restriction to tumour-like spots reduced confounding by RNF19A expression in non-tumour compartments and allowed neighbourhoods to be compared around a common epithelial context.

We next examined immune-related transcriptional programmes surrounding RNF19A-defined tumour-like spots. Spatial mapping revealed substantial heterogeneity in overall immune-cell infiltration, myeloid or tumour-associated macrophage (TAM)-like signatures, T-cell-inhibitory ligands and broader immunosuppressive ligands across the tissue **(Fig. 5D)**. RNF19A-high tumour-like neighbourhoods showed higher suppressive-ligand, T-cell-inhibitory-ligand, myeloid/TAM-like and CD8-exhaustion-like scores than RNF19A-low neighbourhoods **(Fig. 5E-F)**. Thus, tumour regions with high RNF19A expression preferentially occupied spatial niches enriched for suppressive and dysfunctional T-cell-associated programmes.

Consistent with this pattern, RNF19A-high tumour-like spots were frequently located near suppressive-ligand-high spots **(Fig. 5E)**. Nearest-neighbour analysis further showed that RNF19A-high tumour-like spots were closer to suppressive-ligand-high regions than RNF19A-low tumour-like spots (**Supplementary Fig. 7H-I)**. Because these are spot-level observations from one tissue section, they were treated as exploratory spatial associations rather than independently replicated patient-level evidence.

Ligand-receptor programme analysis provided a complementary view of the same neighbourhoods. Several immune-interaction modules differed between RNF19A-high and RNF19A-low regions, including CXCL10-CXCR3, CCL5-receptor, ICAM1-integrin and HLA-CD8-associated programmes **(Fig. 5G)**. The relative enrichment of immune-activating programmes in RNF19A-low neighbourhoods was consistent with the idea that RNF19A-high tumour regions restrained local antitumour communication. Together, the module-score and ligand-receptor analyses indicated that RNF19A status was associated with broad remodelling of immune-related intercellular signalling rather than with a single ligand pair.

Because the spatial analyses pointed particularly to altered CD8 T-cell states, we next focused on CD8-associated programmes. Mapping of CD8 T-cell, exhaustion-like and effector-cytotoxic scores revealed distinct spatial distributions across the CRPC section **(Fig. 5H)**. RNF19A-high tumour-like spots showed preferential spatial association with regions displaying an exhausted CD8-like signature **(Fig. 5I)**. This overlap linked tumour-cell RNF19A expression to a specific dysfunctional T-cell-associated state within the broader suppressive landscape.

To provide an independent cellular reference for these spatial signatures, CRPC CD8 T cells were classified into naive-like, effector-like and exhausted-like states using canonical marker-expression patterns. Naive-like cells expressed LEF1, SELL and CCR7, effector-like cells expressed GZMB and PRF1, and exhausted-like cells were characterized by PDCD1, LAG3 and CTLA4 expression **(Supplementary Fig. 8A-B)**. These transcriptional states were distributed along a branched computational trajectory **(Supplementary Fig. 8C-F)**. The trajectory provided a reference framework for interpreting the spatial CD8-related scores, but it was not used to claim a causal or chronological transition between states.

We finally asked whether altering RNF19A specifically in tumour cells could produce a measurable change in CD8 T cells. Human CD8 T cells were co-cultured with control or RNF19A-depleted prostate-cancer cells, followed by flow-cytometric assessment of PD-1 expression **(Fig. 5J)**. Quantification across three independent experiments showed a significant reduction in the PD-1-positive CD8 T-cell fraction after RNF19A depletion **(Fig. 5K-L)**. This result provided a tumour-cell-directed perturbation that was consistent with the spatial association between RNF19A-high niches and exhaustion-related CD8 T-cell programmes.

Together, these results suggested that high RNF19A expression was associated not only with tumour-cell-intrinsic survival and metabolic programmes, but also with an immune microenvironment enriched for suppressive ligands, myeloid/TAM-like features and dysfunctional CD8 T-cell-associated states. The spatial and co-culture findings therefore supported a model in which tumour-cell RNF19A participates in remodelling tumour-immune interactions during CRPC progression. The next question was which RNF19A-regulated protein could connect this E3 ubiquitin ligase to the immune transcriptional phenotype.

RNF19A controls RELA stability and NF-κB-dependent immune outputs

The preceding analyses suggested that RNF19A influenced both tumour-cell-intrinsic and immune-associated programmes. RNF19A depletion increased TNF-, NF-κB- and other

inflammatory transcriptional programmes, whereas RNF19A-high spatial niches were associated with suppressive and exhausted CD8-like states. Depletion of RNF19A in tumour cells also reduced the PD-1-positive CD8 T-cell fraction in co-culture. Together, these observations raised a mechanistic question: how did tumour-cell RNF19A restrain immune-activating transcriptional outputs and thereby contribute to a suppressive microenvironment?

Because RNF19A is an E3 ubiquitin ligase, we revisited the RNF19A affinity-purification mass-spectrometry dataset to identify candidate substrates that could account for the NF-κB-related transcriptional changes. RELA, the p65 transcriptional subunit of canonical NF-κB, was present among the RNF19A-associated proteins in the enrichment profile **(Fig. 4B)**. RELA therefore represented a direct candidate linking RNF19A-dependent protein turnover to the immune transcriptional phenotype. We consequently examined whether RNF19A physically interacted with RELA and regulated its stability.

RNF19A immunoprecipitation recovered RELA, supporting the presence of the two proteins in the same cellular complex **(Fig. 6A)**. Confocal microscopy further showed substantial spatial overlap between RNF19A and RELA **(Fig. 6B)**. Using purified recombinant proteins, GST-RNF19A retained His-RELA, whereas GST alone did not show comparable retention **(Fig. 6C)**. The agreement between cellular co-immunoprecipitation, colocalization and recombinant pull-down supported a direct RNF19A-RELA interaction. Besides, the results of molecular docking showed that RNF19A predicted interface to RELA (**Supplementary Fig. 9A).** As with p53, these experiments established association but did not define a specific binding interface.

We next asked whether RNF19A regulated RELA abundance. RNF19A depletion increased RELA protein levels, whereas re-expression of RNAi-resistant RNF19A reversed this increase **(Fig. 6D; Supplementary Fig. 9B)**. In contrast, RELA messenger RNA abundance was not detectably altered following RNF19A knockdown **(Supplementary Fig. 9C)**. The protein-transcript separation indicated that RNF19A acted predominantly through post-transcriptional regulation of RELA.

We therefore examined whether RNF19A promoted RELA degradation through the ubiquitin-proteasome system. RNF19A expression reduced RELA protein abundance, and this effect was more effectively reversed by the proteasome inhibitor MG132 than by chloroquine **(Fig. 6E; Supplementary Fig. 9D)**. Consistent with this result, RELA immunoprecipitation followed by ubiquitin Western blot showed that RNF19A depletion reduced the RELA-associated ubiquitin

smear under proteasome-blocking conditions **(Fig. 6F)**. These findings supported RNF19A-dependent ubiquitination and proteasome-associated turnover of RELA, although the ubiquitin-chain linkage and specific modification sites were not determined.

Cycloheximide-chase experiments directly confirmed an effect on RELA stability. Following inhibition of new protein synthesis, RELA declined progressively in control cells, whereas RNF19A depletion delayed RELA loss across the time course **(Fig. 6G-H)**. Thus, RNF19A interacted with RELA, promoted its ubiquitination and accelerated its proteasome-associated turnover. The convergence of rescue, degradation-pathway inhibition, ubiquitination and chase experiments established the same overall proteostasis logic observed for p53, but with a different downstream functional consequence.

Having established RNF19A-dependent regulation of RELA stability, we next asked whether this mechanism accounted for the NF-κB activation observed after RNF19A depletion. RNF19A knockdown markedly increased activity of an NF-κB-responsive luciferase reporter, whereas re-expression of RNAi-resistant RNF19A reduced this increase **(Fig. 6I)**. Importantly, simultaneous RELA silencing also suppressed the reporter response induced by RNF19A depletion. This epistasis-like rescue placed RELA downstream of RNF19A in the regulation of canonical NF-κB transcriptional activity.

We then examined endogenous immune-related genes that could connect this tumour-cell-intrinsic pathway to the spatial phenotype. RNF19A depletion increased expression of the chemokines CXCL10 and CCL5. It also increased genes involved in antigen presentation and immune-cell interaction, including HLA-A, HLA-B, B2M, TAP1, TAP2 and ICAM1, together with STAT1 and IRF1 **(Fig. 6J)**. These findings indicated that the immune transcriptional programme released by RNF19A depletion was substantially RELA dependent rather than a nonspecific consequence of reduced tumour-cell growth.

The transcriptional changes were also reflected at the extracellular protein level. Concentrations of CXCL10 and CCL5 in conditioned medium increased after RNF19A depletion and were reduced by RNF19A rescue or RELA silencing **(Fig. 6K-L)**. Stabilization of RELA following RNF19A loss therefore translated into increased production of soluble immune-activating chemokines. This result provided a plausible route through which tumour-cell RNF19A status could influence surrounding immune cells without requiring direct RNF19A expression in those cells.

Finally, we returned to the tumour-cell/CD8 T-cell co-culture system used to interrogate the spatial observations in Fig. 5. RNF19A depletion reduced the PD-1-positive CD8 T-cell fraction from approximately 20.6% in the shScr condition to 6.17% in the displayed shRNF19A condition. Re-expression of RNF19A partially restored the fraction to approximately 17.0%, whereas RELA silencing attenuated the effect of RNF19A depletion, with a displayed value of approximately 14.8% **(Fig. 6M; Supplementary Fig. 9E)**. These perturbation-rescue relationships linked the tumour-cell RNF19A-RELA axis to the CD8 T-cell phenotype observed in co-culture.

Together, these results provided a mechanistic explanation for the immune-related transcriptional and spatial phenotypes observed in the preceding analyses. RNF19A promoted RELA ubiquitination and proteasome-associated turnover, thereby restraining NF-κB-dependent chemokine, antigen-presentation and immune-interaction programmes in prostate-cancer cells. Conversely, RNF19A depletion stabilized RELA and released these immune-activating outputs. The RNF19A-RELA axis therefore supplied a tumour-cell-intrinsic mechanism linking high RNF19A expression to the suppressive tumour microenvironment associated with CRPC.

Sinomenine binds RNF19A and suppresses prostate-cancer growth

The preceding genetic and mechanistic experiments identified RNF19A as a functional driver of CRPC-associated tumour-cell survival, metabolic adaptation and immune regulation. These findings raised a translational question: whether RNF19A could be pharmacologically targeted and whether such an intervention could reproduce the antitumour phenotypes observed after RNF19A depletion. We therefore performed a structure-guided natural-product screen to identify candidate compounds capable of interacting with RNF19A.

Candidate natural products were first ranked according to their predicted binding energies with RNF19A **(Fig. 7A)**. Six compounds, dihydroxydianthrone, cirrhopetalanthin, chrysanthemaxanthin, palmidin A, physalin A and SIN, were selected for cell-based evaluation **(Fig. 7B; Supplementary Fig. 10A)**. We compared their effects on RNF19A protein abundance and prostate-cancer cell growth in LNCaP and DU145 cells **(Fig. 7C-D)**. Among the tested compounds, SIN consistently reduced RNF19A protein abundance in both cell lines and produced pronounced growth suppression. We therefore prioritized SIN for further investigation.

Molecular docking placed SIN within a predicted binding pocket of RNF19A, with a close interaction predicted near His318 **(Fig. 7B)**. The chemical structure of SIN is shown in **Fig. 7E**, with additional compound views provided in **Supplementary Fig. 10B**. We next examined the

interaction directly using surface plasmon resonance. Recombinant RNF19A showed concentration-dependent binding responses to SIN across the tested range, with a fitted dissociation constant of 5.08×10^{-7} M **(Fig. 7F)**. Together with the computational and cell-based screening results, these data identified SIN as a candidate RNF19A-binding natural product. They did not, however, establish SIN as a selective RNF19A inhibitor.

Having identified SIN as the lead compound, we next asked whether it reproduced the tumour-suppressive phenotypes observed after genetic depletion of RNF19A. SIN progressively reduced CCK-8 signals in both LNCaP and DU145 cells in a concentration- and time-dependent manner **(Supplementary Fig. 10C)**. Consistent with the increased apoptosis observed after RNF19A knockdown, SIN treatment reduced Bcl2 and pro-caspase-3 abundance while increasing cleaved-caspase-3 levels **(Fig. 7G)**. Annexin V-FITC/propidium iodide analysis further demonstrated a concentration-dependent increase in apoptotic cells in both prostate-cancer cell lines **(Fig. 7H-I)**. The protein and flow-cytometric readouts therefore converged on apoptosis as a component of the pharmacological phenotype.

We then extended these observations to a patient-derived model. Treatment of prostate-cancer patient-derived organoids with increasing concentrations of SIN progressively restricted organoid growth, as reflected by reductions in maximum organoid diameter **(Fig. 7J-K)**. Thus, the growth-suppressive activity observed in established cell lines was maintained in a three-dimensional patient-derived tumour model.

We next asked whether the activity of SIN extended to tumour growth in vivo. Mice bearing patient-derived organoid xenografts were treated with vehicle or SIN at 50 or 100 mg/kg. SIN suppressed tumour growth over the treatment period, with a stronger effect at the higher dose **(Fig. 7L)**. Consistently, the excised tumours were smaller and the terminal tumour-weight readouts were reduced in both SIN-treated groups **(Fig. 7L-N)**. These results demonstrated antitumour activity of SIN across prostate-cancer cell lines, patient-derived organoids and an in vivo xenograft model.

Because the RNF19A-RELA axis connected tumour-cell RNF19A to immune-related transcriptional outputs and the CD8 T-cell phenotype, we finally asked whether SIN could reproduce this immune-associated effect. In the tumour-cell/CD8 T-cell co-culture system, increasing concentrations of SIN progressively reduced the PD-1-positive CD8 T-cell fraction **(Fig. 7O; Supplementary Fig. 10D)**. The direction of this response paralleled that observed after

genetic RNF19A depletion and linked the pharmacological intervention back to the immune phenotype identified in the preceding experiments.

Together, these results identified SIN as a candidate RNF19A-binding natural product with antitumour activity in CRPC models. SIN bound recombinant RNF19A, reduced RNF19A protein abundance and reproduced key phenotypes associated with RNF19A depletion. These included impaired tumour-cell growth, increased apoptosis, suppression of patient-derived organoid and xenograft growth, and a reduction in PD-1-positive CD8 T cells. The pharmacological data extended the genetic evidence and supported RNF19A as a potentially actionable vulnerability in CRPC, while further target-engagement and selectivity studies will be required to establish the precise basis of SIN activity.

DISCUSSION

CRPC develops under sustained androgen deprivation and increasingly potent androgen-receptor (AR) pathway inhibition, selecting tumour-cell states that maintain survival, metabolic flexibility and phenotypic adaptability. Genomic and functional studies have implicated alterations in AR, TP53 and RB1, together with lineage plasticity and treatment tolerance, in this process[4-6,16]. Our single-cell comparison identified RNF19A in CRPC-enriched epithelial states, and functional, biochemical, metabolic and immune-associated analyses support a model in which RNF19A contributes to the fitness of these cells through substrate-specific proteostatic control. These data support an association between RNF19A and the castration-resistant state, suggesting that RNF19A may contribute to tumour-cell adaptation by weakening tumour-suppressive constraints and limiting tumour-derived immune-activating outputs.

RNF19A supports CRPC-associated tumour-cell adaptation through proteostatic regulation of p53

RNF19A was previously linked to higher Gleason score, predicted castration resistance and an AR/HIF1A–RNF19A–TRIP13 axis in prostate cancer[14]. Our findings extend this work by showing that RNF19A is enriched in CRPC-associated epithelial states and that its functional consequences include tumour survival, metabolic fitness and immune-related outputs. RNF19A depletion reduced proliferation, clonogenicity, sphere formation and xenograft growth while increasing apoptosis and suppressing ATP biosynthesis, respiration, oxidative phosphorylation and fatty-acid metabolic programmes. These coordinated phenotypes are consistent with RNF19A supporting a stress-adapted tumour-cell state. Substrate dependence is plausible for an RBR E3

ligase: beyond TRIP13, RNF19A regulates BARD1 and interferes with BRCA1/BARD1-dependent homologous recombination[17].

Unbiased RNF19A immunoprecipitation–mass spectrometry identified p53, and subsequent assays supported RNF19A–p53 association, direct interaction and post-transcriptional control. RNF19A depletion increased p53 protein without increasing TP53 mRNA, reduced p53-associated ubiquitination and prolonged p53 stability in a proteasome-dependent manner. RNF19A-mediated p53 degradation has previously been reported in non-small-cell lung cancer[18];our findings extend this relationship to prostate-cancer models in the context of CRPC.

This relationship is relevant because TP53 alterations are enriched in metastatic CRPC, predict adverse clinical behaviour and, together with RB1 loss, promote lineage plasticity and antiandrogen resistance[4-6,16]. RNF19A elevation may provide an additional post-translational route to attenuate p53-dependent restraints.

Lipid and mitochondrial flexibility support treatment-resistant prostate cancer[19,20], consistent with the reduced oxidative and fatty-acid programmes after RNF19A depletion. p53 is one plausible component of this response, but its metabolic effects are context dependent: p53 can support mitochondrial respiration through SCO2[21]while constraining glycolysis and redox imbalance through TIGAR[22].

RNF19A–RELA proteostasis links tumour-cell state to immune-activating outputs

RNF19A-associated adaptation extended beyond tumour-cell-autonomous metabolism. RNF19A depletion increased TNF, NF-κB and broader inflammatory signatures, suggesting that RNF19A may limit the capacity of tumour cells to generate immune-recruiting and immune-recognition signals. This possibility is relevant to CRPC, where IL-23-producing myeloid-derived suppressor cells, hypoxia and SPP1-high tumour-associated macrophages can restrict T-cell activity and contribute to treatment or immune-checkpoint resistance[23-25]. The limited activity of pembrolizumab in unselected treatment-refractory CRPC further illustrates this immunologically restrictive context[10].

RNF19A-high tumour-like regions in the analysed spatial section were associated with suppressive-ligand, myeloid/TAM-like and CD8-exhaustion-like programmes. Tumour-cell perturbation nevertheless offered a mechanistic bridge: RNF19A depletion increased CXCL10 and CCL5, together with HLA-A/B, B2M, TAP1/2 and ICAM1. CXCR3 ligands and CCL5 can cooperate in T-cell recruitment[26], HLA class I, B2M and TAP1/2 support antigen processing and

presentation[27], and ICAM1 facilitates tumour-cell–T-cell contact[28]. Thus, RNF19A-high tumour cells may provide fewer signals for T-cell recruitment, recognition and engagement.

Co-culture experiments supported a tumour-cell-dependent effect: the PD-1-positive CD8 T-cell fraction decreased after RNF19A depletion and was partly restored by RNF19A re-expression. PD-1 alone, however, does not define terminal exhaustion and may also mark recently activated T cells. The data therefore indicate a change in CD8 T-cell state, but do not demonstrate complete reversal of exhaustion or restored tumour-cell killing.

Mechanistically, transcriptomic pathway analysis and unbiased interactomics converged on RELA/p65. RNF19A interacted with RELA, promoted its ubiquitination and proteasome-associated turnover, and restrained NF-κB reporter activity. RNF19A depletion stabilized RELA and induced chemokine, antigen-presentation and adhesion genes, whereas RELA silencing attenuated these responses and the co-culture phenotype. These results place RELA downstream of RNF19A in a tumour-cell immune-activating programme.

NF-κB signalling in CRPC is highly context dependent, with its biological effects influenced by subunit composition, cellular state and stimulus. NF-κB/p52 can activate AR signalling and confer enzalutamide resistance[29,30], and a p65/RELA inflammatory circuit can promote castration resistance under defined conditions[31]. Our results more specifically indicate that RNF19A-mediated RELA turnover suppresses a subset of immune-activating outputs. The reported degradation of TBK1 by RNF19A in antiviral signalling[32] further supports a recurring, substrate-dependent capacity to dampen immune-associated pathways.

Together, the p53 and RELA findings suggest that RNF19A coordinates complementary dimensions of CRPC-associated adaptation. Destabilization of p53 may weaken tumour-suppressive restraints and support survival under treatment stress, with a possible but unproven contribution to metabolism. In parallel, RELA destabilization restricts tumour-derived immune-activating signals and may favour an immunologically restrictive niche. RNF19A may therefore be consequential not because it controls a single dominant pathway, but because substrate-specific turnover couples tumour-cell fitness to immune-evasive communication.

Sinomenine provides a pharmacological entry point into the RNF19A dependency

Natural products provide diverse pharmacologically active scaffolds and have contributed substantially to anticancer drug discovery[33]. Structure-guided screening and cell-based prioritization identified SIN, an isoquinoline alkaloid from Sinomenium acutum with reported

anti-inflammatory and anticancer properties[34], as a candidate RNF19A-binding compound. Docking predicted a compatible pose, surface plasmon resonance supported direct binding to recombinant RNF19A, and treatment reduced RNF19A abundance, impaired tumour-cell and organoid growth, increased apoptosis and inhibited xenograft expansion.

These observations indicate that the genetically defined RNF19A dependency may be chemically accessible, but they do not establish SIN as a selective RNF19A inhibitor. SIN is pharmacologically pleiotropic and modulates several pathways, including NF-κB-related signalling[34,35]. Phenotypic similarity to RNF19A depletion therefore cannot show that all antitumour or immune-associated effects are RNF19A dependent. The therapeutic premise is nevertheless relevant because CRPC remains ultimately lethal despite AR-pathway inhibitors, taxanes, molecularly selected PARP inhibition and PSMA-directed radioligand therapy. Olaparib improves outcomes in patients with homologous-recombination repair alterations[36], and 177Lu-PSMA-617 prolongs survival in selected PSMA-positive CRPC [37], but heterogeneous resistance, metabolic adaptation and immune suppression continue to limit durable control

In summary, RNF19A is associated with CRPC-enriched tumour-cell states and supports prostate cancer growth, metabolic fitness and a RELA-sensitive immune phenotype. The data are consistent with a substrate-specific proteostatic model in which p53 destabilization contributes to tumour-cell adaptation and RELA turnover restricts tumour-derived immune-activating outputs **(Supplementary Fig. 11)**. SIN provides a candidate chemical starting point rather than a validated selective inhibitor. Patient-level spatial validation, p53 metabolic epistasis, cellular RNF19A target engagement and immunocompetent pharmacology are now needed to establish the full causal and therapeutic model.

MATERIALS AND METHODS

Single-cell RNA-seq integration and downstream analysis

Public single-cell RNA-sequencing datasets of hormone-sensitive prostate cancer (HSPC) and CRPC were obtained from GEO (GSE181294, GSE137829 and GSE274229). Raw feature-barcode matrices from GSE274229 were processed in Seurat, with low-quality cells removed according to the number of detected features, UMI counts and mitochondrial transcript proportion, whereas GSE181294 and GSE137829 were incorporated from processed expression objects. Following log normalization and identification of highly variable genes, principal-component analysis was performed and dataset-associated batch effects were reduced using Harmony. UMAP

and t-SNE were used for visualization. Cell identities were assigned using reference-based label transfer together with canonical marker expression. To minimize differences in sampling depth and dataset representation between disease states, cells were balanced within relevant dataset and disease strata before comparative analyses. Cell-cell communication was inferred using CellChat v2.1.2 with CellChatDB.human, and ligand-receptor interactions were aggregated at the signalling-pathway level to characterize incoming and outgoing communication patterns. For analysis of CD8 T-cell states, CRPC T cells expressing CD8-lineage and cytotoxic markers were subsetted, re-normalized and independently integrated with Harmony. Unsupervised clusters were annotated as naive-like, effector-like, proliferating-like or exhausted-like according to canonical marker-set expression. Trajectory inference was performed using Slingshot, with the naive-like state specified as the starting state and the exhausted-like state as the terminal state. Pseudotime was used to describe transcriptional-state relationships rather than to infer causal cell-state transitions. For sample-level differential-expression analyses, biological samples rather than individual cells were treated as the experimental units.

Survival analysis

Patient-level RNF19A expression and survival data were obtained from TCGA-PRAD and publicly available GEO prostate cancer cohorts. Survival outcomes were defined according to the endpoint annotations provided for each cohort. Kaplan–Meier curves were compared using a two-sided log-rank test, and univariable Cox proportional-hazards regression was used to estimate hazard ratios and 95% confidence intervals.

Spatial transcriptomic analysis

Spatial transcriptomic data were obtained from the GEO dataset GSE278936 was used to examine the spatial distribution of RNF19A and associated transcriptional programmes. Spatial gene-expression data were processed in Seurat, with low-quality spots removed according to detected features, total UMI counts and mitochondrial transcript proportions, followed by normalization, dimensionality reduction and clustering. Tumour-associated regions were identified based on tissue annotations and epithelial or prostate cancer marker expression. RNF19A expression and gene-programme or cell-state scores were evaluated across tumour-associated spots to characterize their spatial relationships.

Cell lines and culture

LNCaP clone FGC cells (ATCC, CRL-1740) were maintained in RPMI-1640 medium (ATCC, 30-2001) containing 10% fetal bovine serum. DU145 cells (ATCC, HTB-81) were maintained in Eagle's minimum essential medium (ATCC, 30-2003) containing 10% fetal bovine serum. RWPE-1 cells (ATCC, CRL-3607) were maintained in keratinocyte serum-free medium (Gibco, 17005-042) supplemented with 0.05 mg ml−1 bovine pituitary extract and 5 ng ml−1 epidermal growth factor. Cells were cultured at 37 °C in humidified 5% CO_2.

Transient silencing, stable knockdown and rescue

RNF19A, TP53 and RELA were transiently silenced with target-specific siRNAs, with a non-targeting siRNA used as the negative control. siRNAs were transfected with Lipofectamine RNAiMAX (Invitrogen, 13778150) according to the manufacturer's protocol. Knockdown was assessed by RT-qPCR and Western blot 24–72 h after transfection. For stable RNF19A knockdown, shRNF19A targeting the RNF19A coding sequence was cloned into the pLKO.1-TRC lentiviral backbone through the AgeI and EcoRI sites. A non-targeting shRNA in the same backbone was used as the control. The complete cloning oligonucleotides are listed in **Supplementary Table 4**. Annealed oligonucleotides were ligated into AgeI/EcoRI-digested pLKO.1-TRC, and insert-positive bacterial clones were confirmed by Sanger sequencing before lentivirus production. Antibiotic-selected cell populations were used for subsequent experiments, and knockdown was assessed by RT-qPCR and Western blot. For RNF19A rescue, an RNAi-resistant RNF19A expression construct was introduced with Lipofectamine 3000 (Invitrogen, L3000015), with the matched empty vector used as the control. TP53-silencing rescue experiments combined RNF19A depletion with TP53 siRNA before EdU and metabolic readouts. RELA perturbation was performed in the RNF19A background for NF-κB reporter and inflammatory-gene assays.

RNA isolation, reverse transcription and quantitative PCR

Total RNA was extracted with TRIzol Reagent (Invitrogen, 15596026). cDNA was prepared with PrimeScript RT reagent Kit with gDNA Eraser (Takara, RR047A), including genomic DNA removal at 42 °C for 2 min before reverse transcription according to the manufacturer's protocol. No-reverse-transcriptase and no-template controls were included.

Quantitative PCR was performed with TB Green Premix Ex Taq II, Tli RNaseH Plus (Takara, RR820A). Each 25-µl reaction contained 12.5 µl of 2× mix, 0.4 µM of each primer and no more

than 100 ng template. Two-step cycling was followed by melt-curve analysis. Relative expression was calculated using the 2−ΔΔCt method. Primer sequences are listed in **Supplementary Table 1**.

Bulk RNA sequencing, differential expression and gene-set enrichment

Bulk RNA sequencing was performed using three independently cultured shNC samples and three independently cultured shRNF19A samples. Total RNA extraction, library preparation and sequencing were performed by Guangzhou IGE Biotechnology Co., Ltd. (Guangzhou, China).

Sequencing reads were quality filtered and summarized at the gene level. Differential-expression analysis used the independently cultured samples as biological replicates. Genes were ranked by the differential-expression statistic, and the figure-level fold-change display used |log2 fold change| ≥ 0.5. Gene-set enrichment analysis was performed on the ranked gene list, with correction for multiple testing.

Protein extraction and Western blot

Cells and tissues were lysed on ice in RIPA Lysis and Extraction Buffer (Thermo Fisher Scientific, 89900) supplemented with protease inhibitors and, for phosphorylation assays, phosphatase inhibitors. Protein concentration was measured with the Pierce BCA Protein Assay Kit (Thermo Fisher Scientific, 23225). Equal protein amounts were separated by SDS-PAGE, transferred to membranes, blocked and incubated with the antibodies listed in Supplementary Table 2. HRP-conjugated secondary antibodies and SuperSignal West Pico PLUS substrate (Thermo Fisher Scientific, 34580) were used for detection. Expected apparent masses were approximately 90–91 kDa for canonical RNF19A, 53 kDa for p53, 65 kDa for RELA/p65, 26 kDa for Bcl2, 31 kDa for pro-caspase-3, 17/19 kDa for cleaved caspase-3 and 55 kDa for β-tubulin. Densitometry was performed using unsaturated exposures and normalized to the corresponding loading control.

Anti-FLAG immunoprecipitation and mass spectrometry

Cells expressing FLAG-tagged RNF19A and matched control cells were lysed under non-denaturing conditions with freshly added inhibitors. Cleared lysates were incubated with anti-FLAG antibody and protein A/G beads. Bound proteins were washed, eluted and processed for LC-MS/MS, with the bait-negative control analysed in parallel. LC-MS/MS analysis was performed at the proteomics platform of the University of South China (Hengyang, China).

Candidate interactors were prioritized by enrichment over the bait-negative control, reproducibility and biological relevance. p53 and RELA were subsequently tested by co-immunoprecipitation.

Co-immunoprecipitation, GST pull-down and ubiquitination assays

For co-immunoprecipitation, cells were lysed under non-denaturing conditions with freshly added inhibitors. Clarified lysates were incubated with the indicated antibody or matched IgG, followed by Pierce Protein A/G Magnetic Beads (Thermo Fisher Scientific, 88802). Beads were washed and eluted in SDS sample buffer. Input and IgG controls were analysed in parallel.

GST-tagged proteins were captured with Glutathione Sepharose 4B (Cytiva, 17075601). GST alone and input samples were included as controls.

For ubiquitination assays, p53 or RELA was immunoprecipitated and analysed by Western blot for total, K48-linked and K63-linked ubiquitin.

Cycloheximide chase and degradation-pathway perturbation

Protein stability was assessed after cycloheximide treatment (Selleck Chemicals, S7418). Samples were collected at 0, 12, 24, 36 and 48 h. Target abundance was normalized to the loading control and then to the zero-time sample within each experiment.

Proteasome-associated degradation was examined after treatment with MG132 (Selleck Chemicals, S2619), whereas lysosome- or autophagy-associated degradation was examined using chloroquine diphosphate (Selleck Chemicals, S4157). Vehicle-treated cells were processed in parallel.

Immunofluorescence and mitochondrial imaging

Cells were fixed, permeabilized and blocked before overnight incubation with primary antibodies at 4 °C. Alexa Fluor 488 goat anti-rabbit IgG (Invitrogen, A-11008) and Alexa Fluor 594 goat anti-mouse IgG (Invitrogen, A-11005) were used for detection. Images were acquired with a Zeiss LSM 880 confocal microscope under identical settings within each experiment. For mitochondrial imaging, cells were incubated with 100 nM MitoTracker Orange CMTMRos (Invitrogen, M7510) for 30 min at 37 °C. Cell boundaries and nuclei were counterstained with WGA Alexa Fluor 488 (Invitrogen, W11261) and Hoechst 33342 (Invitrogen, H3570), respectively. For the colocalization images, the Alexa Fluor 488 channel corresponding to RNF19A was pseudocoloured red, whereas the Alexa Fluor 594 channel corresponding to p53 or RELA was pseudocoloured green.

Cell metabolic activity, clonogenic growth and spheroid formation

Cell metabolic activity was assessed with Cell Counting Kit-8 (Dojindo, CK04). After incubation with CCK-8 reagent, absorbance was measured at 450 nm with subtraction of cell-free reagent blanks. For clonogenic assays, cells were seeded at low density and cultured until colonies formed. Colonies were fixed, stained and counted. For spheroid assays, cells were cultured in low-attachment plates, and spheroid number and size were quantified.

Annexin V and TUNEL apoptosis assays

Apoptosis was measured with the BD Pharmingen FITC Annexin V Apoptosis Detection Kit I (BD Biosciences, 556547). Adherent and detached cells were pooled and resuspended at approximately 10^5 cells per 100 µl binding buffer. Cells were stained with 5 µl Annexin V-FITC and 5 µl propidium iodide for 15 min at room temperature in the dark and analysed immediately by flow cytometry. DNA fragmentation in cultured cells and tumour sections was detected with the In Situ Cell Death Detection Kit, Fluorescein (Roche, 11684795910). Cultured cells were fixed and permeabilized before TUNEL labelling. Paraffin sections were deparaffinized, rehydrated and pretreated before labelling. No-TdT and DNase-treated samples served as negative and positive controls, respectively.

Extracellular flux and ATP-production-rate analysis

Cellular ATP production was assessed with an Agilent Seahorse XF Pro Analyzer and the Seahorse XF Real-Time ATP Rate Assay Kit (Agilent, 103592-100). Oxygen consumption rate and extracellular acidification-related measurements were recorded at baseline and after sequential injection of oligomycin and rotenone/antimycin A. Mitochondrial ATP production rate, glycolytic ATP production rate and total ATP production rate were calculated with Seahorse analysis software.

Human CD8 T-cell co-culture and flow cytometry

Primary human CD8 T cells were isolated from peripheral-blood mononuclear cells and co-cultured directly with tumour cells. After co-culture, cells were stained with CD8-FITC (BioLegend, 301006; RPA-T8) and PD-1-APC (BioLegend, 329908; EH12.2H7). Debris and doublets were excluded, and PD-1 expression was quantified within the CD8-positive population.

NF-κB reporter and inflammatory readouts

NF-κB transcriptional activity was measured with pGL4.32[luc2P/NF-κB-RE/Hygro] (Promega, E8491) and the pRL-TK Renilla control plasmid (Promega, E2241). Firefly and Renilla activities were measured with the Dual-Luciferase Reporter Assay System (Promega, E1910), and firefly activity was normalized to Renilla activity within each well. CXCL10, CCL5, HLA-A, HLA-B, B2M, TAP1, TAP2, ICAM1, STAT1 and IRF1 transcripts were quantified by RT-qPCR.

Molecular docking and surface plasmon resonance

Molecular docking was used to evaluate the binding of SIN to RNF19A. Ligand and protein structures were prepared before docking, and the resulting poses were ranked by docking score and inspected for plausible contacts. Surface plasmon resonance analysis of SIN binding to RNF19A was performed by Hubei Ipodix Biotechnology Co., Ltd. (Wuhan, China). SIN was analysed over a concentration range of 12.5–12,800 nM, and sensorgrams were reference- and blank-corrected before fitting.

Sinomenine treatment and patient-derived organoids

SIN hydrochloride (MedChemExpress, HY-15122A) was used for pharmacological experiments. Cells received 0, 5, 20 or 50 μM SIN; SIN at 100 μM was used in selected 24-h immunoblot assays and in CCK-8 time-course assays with measurements up to 96 h. Vehicle-treated cells were processed in parallel, and cell metabolic activity was followed for up to 96 h. Patient-derived prostate-cancer organoids were treated with 0, 5, 20 or 50 μM SIN. Organoid growth or viability was quantified after treatment.

Subcutaneous xenografts, PDOX models and histological analysis

Stable RNF19A-knockdown or control tumour cells were implanted subcutaneously for evaluation of RNF19A loss of function in vivo. Tumour dimensions were measured at the indicated time points, and excised tumours were collected for downstream analyses. Patient-derived organoid xenograft (PDOX) models were established from prostate-cancer organoids. Mice received 0, 50 or 100 mg/kg SIN by intraperitoneal injection, and tumour size was recorded on days 12, 15, 18, 21 and 24. Excised tumours were fixed, paraffin embedded and sectioned for haematoxylin and eosin staining and TUNEL analysis. Sections were imaged and quantified using consistent criteria across groups.

Quantification and statistical analysis

Statistical tests were two-sided unless stated otherwise. Data are shown as individual biological replicates with the summary measure specified in each figure legend. Two groups were compared using paired or unpaired Student's t-tests as appropriate. Welch's correction or a non-parametric alternative was used when assumptions were not met. Three or more groups were analysed by analysis of variance followed by multiple-comparison testing. Repeated tumour measurements were analysed using repeated-measures or mixed-effects models. For single-cell analyses, the biological sample rather than the individual cell was used as the inferential unit for sample-level analyses. Sample-level pseudobulk methods were used for differential expression, and Benjamini-Hochberg correction controlled the false discovery rate in high-dimensional analyses. $P < 0.05$ was considered statistically significant unless otherwise specified.

List of abbreviations

Abbreviation	Full term
APC	Allophycocyanin
AR	Androgen receptor
ATCC	American Type Culture Collection
ATP	Adenosine triphosphate
B2M	Beta-2-microglobulin
BARD1	BRCA1-associated RING domain protein 1
BCA	Bicinchoninic acid
Bcl2	B-cell lymphoma 2
BRCA1	Breast cancer type 1 susceptibility protein
CCK-8	Cell Counting Kit-8
CCL5	C-C motif chemokine ligand 5
CCR7	C-C motif chemokine receptor 7
CD8	Cluster of differentiation 8
cDNA	Complementary DNA
CDS	Coding sequence
CHX	Cycloheximide
CIR	Cirrhopetalanthin
CMX	Chrysanthemaxanthin
CQ	Chloroquine
CRPC	Castration-resistant prostate cancer
CTLA4	Cytotoxic T-lymphocyte-associated protein 4
CXCL10	C-X-C motif chemokine ligand 10
CXCR3	C-X-C motif chemokine receptor 3
DHD	Dihydroxydianthrone
DNA	Deoxyribonucleic acid
ECAR	Extracellular acidification rate
EdU	5-Ethynyl-2'-deoxyuridine
FDR	False discovery rate
FITC	Fluorescein isothiocyanate

Abbreviation	Full term
GC	Guanine and cytosine
GEO	Gene Expression Omnibus
GO	Gene Ontology
GSEA	Gene set enrichment analysis
GST	Glutathione S-transferase
GZMB	Granzyme B
HIF1A	Hypoxia-inducible factor 1 subunit alpha
HLA	Human leukocyte antigen
HLA-A	Human leukocyte antigen A
HLA-B	Human leukocyte antigen B
HRP	Horseradish peroxidase
HSPC	Hormone-sensitive prostate cancer
ICAM1	Intercellular adhesion molecule 1
IF	Immunofluorescence
IgG	Immunoglobulin G
IHC	Immunohistochemistry
IL-23	Interleukin-23
IP	Immunoprecipitation
IRF1	Interferon regulatory factor 1
JAK/STAT	Janus kinase/signal transducer and activator of transcription
K_D	Equilibrium dissociation constant
KEGG	Kyoto Encyclopedia of Genes and Genomes
LAG3	Lymphocyte activation gene 3
LC-MS/MS	Liquid chromatography-tandem mass spectrometry
LEF1	Lymphoid enhancer-binding factor 1
MAPK	Mitogen-activated protein kinase
mRNA	Messenger RNA
mTORC1	Mechanistic target of rapamycin complex 1
NCBI	National Center for Biotechnology Information
NES	Normalized enrichment score
NF-κB	Nuclear factor kappa B

Abbreviation	Full term
OCR	Oxygen consumption rate
p53	Tumour protein p53
Palm A	Palmidin A
PARP	Poly(ADP-ribose) polymerase
PCR	Polymerase chain reaction
PD-1	Programmed cell death protein 1
PDCD1	Programmed cell death 1
PDOX	Patient-derived organoid xenograft
Phy A	Physalin A
PRF1	Perforin 1
PRIDE	PRoteomics IDEntifications
PSMA	Prostate-specific membrane antigen
qPCR	Quantitative polymerase chain reaction
RB1	Retinoblastoma transcriptional corepressor 1
RBR	RING-between-RING
RELA	RELA proto-oncogene, NF-κB subunit (p65)
RIPA	Radioimmunoprecipitation assay
RNA	Ribonucleic acid
RNA-seq	RNA sequencing
RNAi	RNA interference
RNF19A	Ring finger protein 19A
RPMI-1640	Roswell Park Memorial Institute 1640 medium
RT-qPCR	Reverse transcription quantitative polymerase chain reaction
SCO2	SCO2 cytochrome c oxidase assembly protein
scRNA-seq	Single-cell RNA sequencing
SDS	Sodium dodecyl sulfate
SDS-PAGE	Sodium dodecyl sulfate-polyacrylamide gel electrophoresis
SELL	Selectin L
SEM	Standard error of the mean
shNC	Non-targeting short hairpin RNA control
shRNA	Short hairpin RNA

Abbreviation	Full term
shScr	Scrambled short hairpin RNA control
si-NC	Non-targeting small interfering RNA control
SIN	Sinomenine
siRNA	Small interfering RNA
SPP1	Secreted phosphoprotein 1
STAT1	Signal transducer and activator of transcription 1
t-SNE	t-Distributed stochastic neighbour embedding
TAM	Tumour-associated macrophage
TAP1	Transporter associated with antigen processing 1
TAP2	Transporter associated with antigen processing 2
TBK1	TANK-binding kinase 1
TCGA-PRAD	The Cancer Genome Atlas Prostate Adenocarcinoma
TdT	Terminal deoxynucleotidyl transferase
TIGAR	TP53-induced glycolysis regulatory phosphatase
TNF	Tumour necrosis factor
TP53	Tumour protein p53 gene
TRIP13	Thyroid hormone receptor interactor 13
TUNEL	Terminal deoxynucleotidyl transferase dUTP nick-end labelling
UMAP	Uniform manifold approximation and projection
UMI	Unique molecular identifier
WB	Western blotting
WGA	Wheat germ agglutinin

Declarations

Ethics approval and consent to participate

All animal procedures were conducted in accordance with the ethical standards and applicable guidelines of the University of South China. The animal experiments were approved by the Animal Ethics Committee of the University of South China (approval no. NHDLS202607029).

Consent for publication

Not applicable.

Availability of data and materials

The single-cell RNA sequencing (scRNA-seq) data generated in this study have been deposited in the NCBI Gene Expression Omnibus (GEO) under accession number GSE326296. During peer review, these data are accessible to reviewers through GEO reviewer access. The mass spectrometry proteomics data have been deposited with the ProteomeXchange Consortium via the PRIDE partner repository under dataset identifier PXD082903.

Competing interests

The authors declare that they have no competing interests.

Funding

This work was supported by the National Natural Science Foundation of China (grant no. 32470886 to PL) and a key grant from the Natural Science Foundation of Hunan Province (grant no. 2025JJ30012 to PL).

Authors' contributions

ZD and HL contributed to investigation, data curation, validation, and formal analysis. SX performed bioinformatics analysis and visualization. MX, YH, TJ, PF, XZ, ZL, WX, and YD contributed to investigation, methodology, and validation. PL and NY conceived and supervised the study, administered the project, acquired funding, and revised the manuscript. ZD drafted the manuscript. All authors read and approved the final manuscript.

Acknowledgements

The authors thank the members of the Lu laboratory for their insightful discussions. The authors also thank the Molecular Imaging Core Facility and the Molecular and Cell Biology Core Facility at Hengyang Medical School, University of South China, for technical assistance.

REFERENCES

1 Bray, F. *et al.* Global cancer statistics 2022: GLOBOCAN estimates of incidence and mortality worldwide for 36 cancers in 185 countries. *CA: a cancer journal for clinicians* **74**, 229-263, doi:10.3322/caac.21834 (2024).

2 de Bono, J. S. *et al.* Abiraterone and increased survival in metastatic prostate cancer. *The New England journal of medicine* **364**, 1995-2005, doi:10.1056/NEJMoa1014618 (2011).

3 Scher, H. I. *et al.* Increased survival with enzalutamide in prostate cancer after chemotherapy. *The New England journal of medicine* **367**, 1187-1197, doi:10.1056/NEJMoa1207506 (2012).

4 Robinson, D. *et al.* Integrative clinical genomics of advanced prostate cancer. *Cell* **161**, 1215-1228, doi:10.1016/j.cell.2015.05.001 (2015).

5 Ku, S. Y. *et al.* Rb1 and Trp53 cooperate to suppress prostate cancer lineage plasticity, metastasis, and antiandrogen resistance. *Science (New York, N.Y.)* **355**, 78-83, doi:10.1126/science.aah4199 (2017).

6 Mu, P. *et al.* SOX2 promotes lineage plasticity and antiandrogen resistance in TP53- and RB1-deficient prostate cancer. *Science (New York, N.Y.)* **355**, 84-88, doi:10.1126/science.aah4307 (2017).

7 Chan, J. M. *et al.* Lineage plasticity in prostate cancer depends on JAK/STAT inflammatory signaling. *Science (New York, N.Y.)* **377**, 1180-1191, doi:10.1126/science.abn0478 (2022).

8 He, M. X. *et al.* Transcriptional mediators of treatment resistance in lethal prostate cancer. *Nature medicine* **27**, 426-433, doi:10.1038/s41591-021-01244-6 (2021).

9 Kiviaho, A. *et al.* Single cell and spatial transcriptomics highlight the interaction of club-like cells with immunosuppressive myeloid cells in prostate cancer. *Nature communications* **15**, 9949, doi:10.1038/s41467-024-54364-1 (2024).

10 Antonarakis, E. S. *et al.* Pembrolizumab for Treatment-Refractory Metastatic Castration-Resistant Prostate Cancer: Multicohort, Open-Label Phase II KEYNOTE-199 Study. *Journal of clinical oncology : official journal of the American Society of Clinical Oncology* **38**, 395-405, doi:10.1200/jco.19.01638 (2020).

11 Xu, P. *et al.* Androgen receptor blockade resistance with enzalutamide in prostate cancer results in immunosuppressive alterations in the tumor immune

microenvironment. *Journal for immunotherapy of cancer* **11**, doi:10.1136/jitc-2022-006581 (2023).

12 An, J., Wang, C., Deng, Y., Yu, L. & Huang, H. Destruction of full-length androgen receptor by wild-type SPOP, but not prostate-cancer-associated mutants. *Cell reports* **6**, 657-669, doi:10.1016/j.celrep.2014.01.013 (2014).

13 Atanasov, A. G., Zotchev, S. B., Dirsch, V. M. & Supuran, C. T. Natural products in drug discovery: advances and opportunities. *Nature reviews. Drug discovery* **20**, 200-216, doi:10.1038/s41573-020-00114-z (2021).

14 Zhang, N. *et al.* CRISPR screening reveals gleason score and castration resistance related oncodriver ring finger protein 19 A (RNF19A) in prostate cancer. *Drug Resist Updat* **67**, 100912, doi:10.1016/j.drup.2022.100912 (2023).

15 Luo, L. *et al.* Molecular cloning and preliminary functional analysis of six RING-between-ring (RBR) genes in grass carp (Ctenopharyngodon idellus). *Fish Shellfish Immunol* **87**, 62-72, doi:10.1016/j.fsi.2018.12.078 (2019).

16 Abida, W. *et al.* Genomic correlates of clinical outcome in advanced prostate cancer. *Proceedings of the National Academy of Sciences of the United States of America* **116**, 11428-11436, doi:10.1073/pnas.1902651116 (2019).

17 Zhu, Q. *et al.* RNF19A-mediated ubiquitination of BARD1 prevents BRCA1/BARD1-dependent homologous recombination. *Nature communications* **12**, 6653, doi:10.1038/s41467-021-27048-3 (2021).

18 Cheng, Y. *et al.* Ring finger protein 19A is overexpressed in non-small cell lung cancer and mediates p53 ubiquitin-degradation to promote cancer growth. *Journal of cellular and molecular medicine* **25**, 7796-7808, doi:10.1111/jcmm.16674 (2021).

19 Blomme, A. *et al.* THEM6-mediated reprogramming of lipid metabolism supports treatment resistance in prostate cancer. *EMBO molecular medicine* **14**, e14764, doi:10.15252/emmm.202114764 (2022).

20 Liu, S. *et al.* Acetyl-CoA carboxylase 1 depletion suppresses de novo fatty acid synthesis and mitochondrial β-oxidation in castration-resistant prostate cancer cells. *The Journal of biological chemistry* **299**, 102720, doi:10.1016/j.jbc.2022.102720 (2023).

21 Matoba, S. *et al.* p53 regulates mitochondrial respiration. *Science (New York, N.Y.)* **312**, 1650-1653, doi:10.1126/science.1126863 (2006).

22 Bensaad, K. *et al.* TIGAR, a p53-inducible regulator of glycolysis and apoptosis. *Cell* **126**, 107-120, doi:10.1016/j.cell.2006.05.036 (2006).

23 Calcinotto, A. *et al.* IL-23 secreted by myeloid cells drives castration-resistant prostate cancer. *Nature* **559**, 363-369, doi:10.1038/s41586-018-0266-0 (2018).

24 Jayaprakash, P. *et al.* Targeted hypoxia reduction restores T cell infiltration and sensitizes prostate cancer to immunotherapy. *The Journal of clinical investigation* **128**, 5137-5149, doi:10.1172/jci96268 (2018).

25 Lyu, A. *et al.* Evolution of myeloid-mediated immunotherapy resistance in prostate cancer. *Nature* **637**, 1207-1217, doi:10.1038/s41586-024-08290-3 (2025).

26 Dangaj, D. *et al.* Cooperation between Constitutive and Inducible Chemokines Enables T Cell Engraftment and Immune Attack in Solid Tumors. *Cancer cell* **35**, 885-900.e810, doi:10.1016/j.ccell.2019.05.004 (2019).

27 Gettinger, S. *et al.* Impaired HLA Class I Antigen Processing and Presentation as a Mechanism of Acquired Resistance to Immune Checkpoint Inhibitors in Lung Cancer. *Cancer discovery* **7**, 1420-1435, doi:10.1158/2159-8290.Cd-17-0593 (2017).

28 Ueda, R. *et al.* Dicer-regulated microRNAs 222 and 339 promote resistance of cancer cells to cytotoxic T-lymphocytes by down-regulation of ICAM-1. *Proceedings of the National Academy of Sciences of the United States of America* **106**, 10746-10751, doi:10.1073/pnas.0811817106 (2009).

29 Nadiminty, N. *et al.* Aberrant activation of the androgen receptor by NF-kappaB2/p52 in prostate cancer cells. *Cancer research* **70**, 3309-3319, doi:10.1158/0008-5472.Can-09-3703 (2010).

30 Nadiminty, N. *et al.* NF-κB2/p52 induces resistance to enzalutamide in prostate cancer: role of androgen receptor and its variants. *Molecular cancer therapeutics* **12**, 1629-1637, doi:10.1158/1535-7163.Mct-13-0027 (2013).

31 Jeong, J. H., Park, S. J., Dickinson, S. I. & Luo, J. L. A Constitutive Intrinsic Inflammatory Signaling Circuit Composed of miR-196b, Meis2, PPP3CC, and p65 Drives Prostate Cancer Castration Resistance. *Molecular cell* **65**, 154-167, doi:10.1016/j.molcel.2016.11.034 (2017).

32 Yang, Y., Cao, X., Huang, L. & Yang, A. RNF19a inhibits antiviral immune response to RNA viruses through degradation of TBK1. *Molecular immunology* **143**, 1-6, doi:10.1016/j.molimm.2021.12.021 (2022).

33 Newman, D. J. & Cragg, G. M. Natural Products as Sources of New Drugs over the Nearly Four Decades from 01/1981 to 09/2019. *Journal of natural products* **83**, 770-803, doi:10.1021/acs.jnatprod.9b01285 (2020).

34 Zhang, Z. *et al.* CGI1746 targets sigma(1)R to modulate ferroptosis through mitochondria-associated membranes. *Nat Chem Biol* **20**, 699-709, doi:10.1038/s41589-023-01512-1 (2024).

35 Song, L. *et al.* Sinomenine inhibits breast cancer cell invasion and migration by suppressing NF-κB activation mediated by IL-4/miR-324-5p/CUEDC2 axis. *Biochemical and biophysical research communications* **464**, 705-710, doi:10.1016/j.bbrc.2015.07.004 (2015).

36 de Bono, J. *et al.* Olaparib for Metastatic Castration-Resistant Prostate Cancer. *The New England journal of medicine* **382**, 2091-2102, doi:10.1056/NEJMoa1911440 (2020).

37 Sartor, O. *et al.* Lutetium-177-PSMA-617 for Metastatic Castration-Resistant Prostate Cancer. *The New England journal of medicine* **385**, 1091-1103, doi:10.1056/NEJMoa2107322 (2021).

38 Perez-Riverol, Y. *et al.* The PRIDE database at 20 years: 2025 update. *Nucleic Acids Res* **53**, D543-D553, doi:10.1093/nar/gkae1011 (2025).

FIGURE LEGENDS

Figure 1 | Integrated single-cell analyses and multidimensional screening identify RNF19A as a CRPC-associated E3 ubiquitin ligase.

(A) Overview of the analytical workflow integrating single-cell transcriptomics, cell-cell communication, basal-cell pseudobulk differential expression, candidate intersection and survival analysis. (B) t-SNE representation of the balanced atlas coloured by disease state. (C) t-SNE representation coloured by the nine major cell classes (12 HSPC and 12 CRPC samples; 78,758 cells). (D) Cell–cell communication networks showing interaction number (left) and interaction strength (right) in HSPC (top) and CRPC (bottom). (E) Incoming and outgoing interaction strengths across cell classes in HSPC and CRPC. (F) Differential interaction number and strength between disease states. (G) Sample-level pseudobulk differential expression in basal-like epithelial cells (HSPC, n = 17 samples; CRPC, n = 5 samples; edgeR quasi-likelihood analysis; FDR < 0.05 and |log2 fold change| ≥ 1). (H) Intersection of CRPC-associated genes, annotated E3 ubiquitin ligases, survival-associated genes and relatively unexplored genes, identifying RNF19A. (I) Kaplan-Meier analysis stratified by RNF19A expression (hazard ratio, 1.80; 95% confidence interval, 1.24-2.61; two-sided log-rank P = 0.0017). HSPC, hormone-sensitive prostate cancer; CRPC, castration-resistant prostate cancer; FDR, false-discovery rate.

Figure 2 | RNF19A supports prostate cancer cell proliferation, survival and androgen-independent tumour growth.

(A) Western blot analysis of RNF19A expression in RWPE-1, LNCaP and DU145 cells. (B) Representative colony-formation assays after RNF19A silencing. (C-D) Representative spheroids and sphere-number quantification after RNF19A silencing; scale bar, 100 μm. (E-F) Representative Annexin V-FITC/propidium iodide plots and apoptotic-cell quantification. (G) Representative western blotting results showing the expression of Bcl2, pro-caspase-3 and cleaved caspase-3 in LNCaP and DU145 cells transfected with si-NC or si-RNF19A. (H) Quantification of cleaved caspase-3 protein expression normalized to β-tubulin and presented relative to the corresponding si-NC group. Data are presented as mean ± SEM (n = 3). $^{*}P < 0.05$, $^{**}P < 0.01$. (I-J) Representative TUNEL staining and quantification of TUNEL-positive cells; scale bar, 50 μm. Data are presented as mean ± SEM (n = 3). $^{**}P < 0.01$, $^{***}P < 0.001$. (K) Stable-knockdown

xenograft workflow. (L) Excised shScr and shRNF19A tumours (n = 3 per group). (M-N) Tumour-volume trajectories and terminal tumour-weight readouts. Data are presented as mean ± SEM (n = 3). $^{*}P < 0.05$, $^{****}P < 0.0001$. (O-P) Haematoxylin-and-eosin staining and tumour-compactness quantification. Data are presented as mean ± SEM (n = 3). $^{*}P < 0.05$. (Q-R) RNF19A immunofluorescence and mean-intensity quantification; scale bar, 50 μm. Data are presented as mean ± SEM (n = 3). $^{***}P < 0.001$. (S) Quantification of TUNEL-positive cells in xenograft tumours. . Data are presented as mean ± SEM (n = 3). $^{*}P < 0.05$.

Figure 3 | RNA-seq and metabolic assays reveal that RNF19A sustains energy metabolism in prostate cancer cells.

(A-B) GO and KEGG enrichment among genes associated with RNF19A-high basal-like epithelial cells. (C-D) Volcano plot and heatmap of bulk RNA-sequencing data from independently cultured shScr and shRNF19A samples (n = 3 per group). (E-F) GO and KEGG enrichment of transcriptional changes after RNF19A depletion. (G) Gene-set enrichment analysis showing significant depletion of glycolysis (NES = −0.87, FDR = 0.021), mitochondrial respiration (NES = −1.89, FDR = 6×10^{-4}), mTORC1 signalling (NES = −0,82, FDR = 0.045) and oxidative phosphorylation (NES = −1.23, FDR = 7.3×10^{-4}). (H) Extracellular-acidification rate (ECAR) and oxygen-consumption rate (OCR) in LNCaP and DU145 cells after RNF19A depletion; oligomycin and rotenone/antimycin A were injected as indicated. (I) Mitochondrial ATP and glycolytic ATP production rates calculated from the extracellular-flux measurements. Data are presented as mean ± SEM (n = 6). $^{***}P < 0.001$, $^{****}P < 0.0001$. (J-K) Hoechst/WGA/MitoTracker Orange imaging and relative MitoTracker-fluorescence quantification; scale bar, 10 μm. Data are presented as mean ± SEM (n = 3), $^{**}P < 0.01$. NES, normalized enrichment score; FDR, false-discovery rate.

Figure 4 | RNF19A interacts with p53 and promotes its ubiquitin-proteasome-dependent degradation.

(A) Overlap of proteins detected by RNF19A affinity-purification mass spectrometry and the matched control. (B) Enrichment profile highlighting RNF19A-associated proteins, including p53 and RELA. (C) Reciprocal co-immunoprecipitation of RNF19A and p53. (D) Confocal colocalization of RNF19A and p53; scale bar, 20 μm. (E) GST pull-down of recombinant GST-

RNF19A and His-p53. RNF19A and p53 are displayed in red and green, respectively, using pseudocolours; nuclei are shown in blue. (F-G) p53 and RNF19A protein abundance and densitometric quantification after RNF19A depletion and RNAi-resistant RNF19A rescue in LNCaP cells. Data are presented as mean ± SEM (n = 3). $^{***}P < 0.001$. (H) p53 mRNA after RNF19A depletion. (I-J) Effects of MG132 and chloroquine on RNF19A-associated p53 loss and densitometric quantification. Data are presented as mean ± SEM (n = 3). $^{***}P < 0.001$. (K-L) p53-associated ubiquitination and quantification after RNF19A depletion and RNF19A rescue. Data are presented as mean ± SEM (n = 3). $^{***}P < 0.001$. (M-N) LNCaP cells expressing shScr or shRNF19A were treated with CHX and harvested at the indicated time points (0, 12, 24, 36, and 48 h). Densitometric quantification of p53 protein levels. Data are presented as mean ± SEM (n = 3). $^{***}P < 0.001$. CQ, chloroquine; CHX, cycloheximide.

Figure 5 | RNF19A-high tumour regions are associated with suppressive immune programmes.

(A) Tissue-region annotation of a quality-controlled CRPC spatial transcriptomic section. (B) UMAP representation of spatial spots. (C) Spatial RNF19A expression and classification of tumour-like spots as RNF19A-high, RNF19A-medium or RNF19A-low. (D) Spatial module scores for immune infiltration, myeloid/TAM-like states, T-cell-inhibitory ligands and immunosuppressive ligands. (E) Spatial overlap of RNF19A-high tumour-like spots and suppressive-ligand-high spots. (F) Neighbourhood programme scores around RNF19A-high and RNF19A-low tumour-like spots; all displayed comparisons have $P < 0.0001$. (G) Relative representation of antitumour ligand-receptor programmes, including CXCL10-CXCR3, CCL5-receptor, ICAM1-integrin and HLA-CD8-associated interactions, in Log_2 fold changes in gene expression comparing RNF19A-high with RNF19A-low spots. (H) Spatial CD8 T-cell, exhaustion-like and effector-cytotoxic programmes. (I) Overlap between RNF19A-high tumour-like spots and exhausted-CD8-like regions. Spatial analyses are exploratory spot-level associations from one tissue section and do not represent independent patient replication. (J) Tumour-cell/CD8+ T-cell co-culture workflow. (K-L) Representative flow-cytometry plots and quantification of PD-1+ cells among CD8+ T cells after tumour-cell RNF19A depletion. Data are presented as mean ± SEM (n = 3). $^{*}P < 0.05$. TAM, tumour-associated macrophage.

Figure 6 | RNF19A promotes RELA ubiquitination and suppresses NF-κB-dependent immune activation outputs in CRPC tumour cells.

(A) Co-immunoprecipitation of RNF19A and RELA. (B) Confocal colocalization of RNF19A and RELA; scale bar, 20 μm. RNF19A and RELA are displayed in red and green, respectively, using pseudocolours; nuclei are shown in blue. (C) GST pull-down of recombinant GST-RNF19A and His-RELA. (D) RELA and RNF19A protein abundance after RNF19A depletion and RNAi-resistant RNF19A rescue. (E) Effects of MG132 and chloroquine on RNF19A-associated RELA loss. (F) RELA-associated ubiquitination after RNF19A depletion under proteasome-blocking conditions. (G-H) LNCaP cells expressing shScr or shRNF19A were treated with CHX and harvested at the indicated time points (0, 12, 24, 36, and 48 h). Densitometric quantification of RELA protein levels. Data are presented as mean ± SEM (n = 3). $^{*}P < 0.05$, $^{***}P < 0.001$. (I) NF-κB reporter activity after RNF19A depletion, RNF19A rescue or RELA silencing. Data are presented as mean ± SEM (n = 3). $^{***}P < 0.001$. (J) RT-qPCR analysis of CXCL10, CCL5, HLA-A, HLA-B, B2M, TAP1, TAP2, ICAM1, STAT1 and IRF1. Data are presented as mean ± SEM (n = 3). $^{*}P < 0.05$, $^{**}P < 0.01$, $^{***}P < 0.001$. (K-N) CXCL10 and CCL5 concentrations in conditioned medium after RNF19A depletion, RNF19A rescue or RELA silencing. Data are presented as mean ± SEM (n = 6). $^{***}P < 0.001$. (M) PD-1+ CD8+ T-cell fraction in tumour-cell/T-cell co-culture after RNF19A depletion, RNF19A rescue or RELA silencing. Data are presented as mean ± SEM (n = 3). $^{*}P < 0.05$.

Figure 7 | Sinomenine is identified as a candidate RNF19A-binding natural product and suppresses CRPC tumour growth. (A) Predicted RNF19A-binding-energy distribution and the ten highest-ranked natural products. (B) Predicted SIN-binding pose near RNF19A His318. (C) Representative western blot analysis of RNF19A protein levels in LNCaP and DU145 cells treated with the indicated compounds. (D) CCK-8 growth profiles after candidate-compound treatment. (E) Chemical structure of SIN. (F) Surface-plasmon-resonance sensorgrams for SIN binding to recombinant RNF19A (12.5-12,800 nM; fitted KD = 5.08×10^{-7} M). (G) Bcl2, pro-caspase-3 and cleaved caspase-3 immunoblots after 24 h of SIN exposure (0-100 μM). (H-I) Representative Annexin V-FITC/propidium iodide plots and apoptotic-cell quantification after SIN treatment (0, 5, 20 or 50 μM). Data are presented as mean ± SEM (n = 3). $^{*}P < 0.05$, $^{**}P < 0.01$, $^{***}P < 0.001$. (J-K) Representative patient-derived prostate-cancer organoids and maximum-diameter

quantification after SIN treatment; scale bar, 100 μm. Data are presented as mean ± SEM (n = 3). $^{*}P < 0.05$, $^{***}P < 0.001$. (L-N) Excised patient-derived organoid xenografts, tumour-volume trajectories and terminal tumour-weight readouts after vehicle or SIN treatment (50 or 100 mg/kg; n = 3 per group). Data are presented as mean ± SEM (n = 3). $^{*}P < 0.05$, $^{**}P < 0.01$, $^{***}P < 0.001$, $^{****}P < 0.0001$. (O) PD-1+ CD8+ T-cell fraction after SIN treatment in tumour-cell/T-cell co-culture. Data are presented as mean ± SEM (n = 3). $^{*}P < 0.05$, $^{**}P < 0.01$.

SUPPLEMENTARY FIGURE LEGENDS

Supplementary Figure 1 | Integrated single-cell analysis and multidimensional screening identify RNF19A as a CRPC-associated E3 ubiquitin ligase.

(A) t-SNE representation coloured by sample source for the balanced 12-HSPC/12-CRPC atlas. (B) Unsupervised clusters at resolution 0.75. (C) Canonical marker-expression dot plot used to evaluate the major cell annotations. (D) Total inferred interaction number and aggregate interaction strength in HSPC and CRPC. (E) Contribution of outgoing communication patterns across cell classes. (F) Outgoing signalling-pathway heatmaps by disease state. (G) Absolute and relative pathway information flow. (H) RNF19A expression on the embedding and descriptive cell-level comparison in basal-like epithelial cells ($P = 8.60 \times 10^{-10}$). The cell-level comparison is descriptive and was not treated as patient-level inference.

Supplementary Figure 2 | RNF19A is upregulated in prostate cancer cells and efficiently silenced by siRNAs.

(A-B) RNF19A mRNA and protein abundance in RWPE-1, LNCaP and DU145 cells. Data are presented as mean ± SEM (n = 3). $^{*}P < 0.05$, $^{**}P < 0.01$. (C-H) RT-qPCR, Western blot and densitometric validation of three independent RNF19A-targeting siRNAs in LNCaP and DU145 cells. Data are presented as mean ± SEM (n = 3). $^{*}P < 0.05$, $^{**}P < 0.01$, $^{***}P < 0.001$. (I) CCK-8 time courses after RNF19A silencing. Data are presented as mean ± SEM (n = 3). $^{****}P < 0.0001$. (J) Colony-formation efficiency. Data are presented as mean ± SEM (n = 3). $^{**}P < 0.01$ (K-L) Densitometric quantification of Bcl2 and pro-caspase-3 signals after RNF19A silencing. Data are presented as mean ± SEM (n = 3). $^{**}P < 0.01$, $^{***}P < 0.001$.

Supplementary Figure 3 | Stable RNF19A knockdown suppresses long-term prostate cancer cell growth and promotes apoptosis in xenograft tumours.

(A) RT-qPCR validation of stable shRNA-mediated RNF19A knockdown in LNCaP and DU145 cells. Data are presented as mean ± SEM (n = 3). $^{*}P < 0.05$, $^{**}P < 0.01$. (B-C) Representative colony-formation assays and colony-formation efficiency in shScr and shRNF19A cells. Data are presented as mean ± SEM (n = 3). $^{**}P < 0.01$, $^{***}P < 0.001$. (D) CCK-8 time courses in stable-knockdown cells. Data are presented as mean ± SEM (n = 3). $^{*}P < 0.05$, $^{***}P < 0.001$, $^{****}P$

< 0.0001. (E) Mice bearing control or RNF19A-depleted subcutaneous tumours. (F) Representative tumour TUNEL staining.

Supplementary Figure 4 | RNF19A-high tumour epithelial cells are associated with metabolic and immune-related programs.

(A) Single-cell t-SNE display of RNF19A-high and RNF19A-low basal-like epithelial cells. (B) Cell-level differential-expression volcano plot.

Supplementary Figure 5 | GO and KEGG enrichment of upregulated genes after RNF19A knockdown. (A-B) GO and KEGG enrichment among upregulated genes meeting the displayed log2 fold-change threshold. Dot position indicates gene ratio, dot size indicates gene count and colour indicates $-\log_{10}^{FDR}$. FDR, false-discovery rate.

Supplementary Figure 6 | Supporting evidence for RNF19A-mediated regulation of p53 protein stability. (A-B) p53 protein abundance and densitometric quantification in RWPE-1, LNCaP and DU145 cells. Data are presented as mean ± SEM (n = 3). $^{**}P < 0.01$. (C) Predicted interaction between RNF19A and p53 based on molecular docking analysis. (D) Quantification showing RNF19A in LNCaP cells. Data are presented as mean ± SEM (n = 3). $^{***}P < 0.001$. (E-F) Western blot and quantification showing p53 and RNF19A in DU145 cells after RNF19A depletion and RNAi-resistant RNF19A rescue. Data are presented as mean ± SEM (n = 3). $^{**}P < 0.01$, $^{***}P < 0.001$. (G-H) Effects of MG132 and chloroquine on RNF19A-associated p53 loss and densitometric quantification in DU145 cells. Data are presented as mean ± SEM (n = 3). $^{***}P < 0.001$.

Supplementary Figure 7 | Spatial transcriptomic quality control and RNF19A-high tumour like spot definition.

(A) Spatial maps of UMI count, detected features and mitochondrial-transcript proportion. (B-C) Distributions of total counts and mitochondrial-transcript proportion. (D-E) UMAP and spatial distribution of transcriptomic clusters. (F) Epithelial, fibroblast, myeloid and T-cell module scores. (G) Preliminary tissue-region annotation. (H) Nearest distance from RNF19A-high and RNF19A-low tumour-like spots to suppressive-ligand-high spots (P = 0.0021; Benjamini-

Hochberg-adjusted P = 0.0041). (I) Empirical cumulative distribution of nearest-neighbour distances. Analyses are exploratory spot-level associations from one section.

Supplementary Figure 8 | Single-cell trajectory analysis of CD8 T-cell exhaustion in CRPC.

(A) Marker-expression dot plot for naive-like, effector-like and exhausted-like CD8 T-cell states. (B) t-SNE representation of the annotated states. (C-D) Slingshot trajectories and pseudotime, with the naive-like state specified as the starting state. (E-F) Cluster- and branch-associated expression heatmaps, including RNF19A. Pseudotime describes transcriptional-state relationships and does not establish causal transitions.

Supplementary Figure 9 | Additional validation of RNF19A-mediated RELA destabilization and RELA-dependent immune activation outputs.

(A) Predicted interaction between RNF19A and RELA based on molecular docking analysis. (B) RELA densitometric quantification after RNF19A depletion and RNAi-resistant RNF19A rescue in LNCaP cells. Data are presented as mean ± SEM (n = 3). $^{*}P < 0.05$, $^{**}P < 0.01$. (C) RELA mRNA after RNF19A depletion. (D) RELA protein quantification after chloroquine or MG132 treatment. Data are presented as mean ± SEM (n = 3). $^{**}P < 0.01$. (E) Representative flow-cytometry plots of PD-1 expression among CD8+ T cells after co-culture with shScr, shRNF19A, RNF19A-rescued or RELA-silenced tumour cells.

Supplementary Figure 10 | Additional validation of natural product docking, sinomenine activity, and RNF19A-RELA-dependent regulation of PD-1+ CD8 T cells.

(A) Predicted RNF19A-binding poses for CMX, DHD, CIR, Palm A and Phy A. (B) Three-dimensional structure of SIN. (C) CCK-8 in LNCaP and DU145 cells treated with the indicated SIN concentrations. Data are presented as mean ± SEM (n = 3). $^{****}P < 0.0001$. (D) Representative flow-cytometry plots of PD-1 expression among CD8+ T cells after tumour-cell treatment with 0, 5, 20 or 50 μM SIN. SIN: sinomenine; CMX: chrysanthemaxanthin; DHD: dihydroxydianthrone; CIR: cirrhopetalanthin; Palm A: palmidin A; Phy A: physalin A.

Supplementary Figure 11 | Proposed model of RNF19A function in CRPC.

Conceptual model in which CRPC-associated RNF19A promotes the ubiquitination and proteasome-associated turnover of p53 and RELA, thereby supporting tumour-cell survival and metabolic fitness while restricting RELA-dependent tumour-derived immune-activating outputs. SIN is shown as a candidate RNF19A-binding chemical starting point. The schematic summarizes the proposed model and does not imply that every depicted intermediate has been causally validated.

Supplementary Table 1 | Primer sequences and expected amplicon sizes for qPCR.

Sequences and expected amplicon sizes of primers used for quantitative PCR (qPCR). All primer sequences are listed in the 5′ to 3′ direction. F and R denote forward and reverse primers, respectively; bp, base pairs.

Supplementary Table 2 | Antibodies used in this study.

Antibody information includes the target, supplier, catalog number, host species and clonality, and applications with working conditions. WB, Western blotting; IHC, immunohistochemistry; IF, immunofluorescence; IP, immunoprecipitation. Antibody dilutions and quantities are indicated as shown.

Supplementary Table 3 | Key resources and reagents used in this study.

The table lists the resources and reagents, suppliers, catalog numbers, and purposes or applications. ATCC, American Type Culture Collection; qPCR, quantitative polymerase chain reaction; siRNA, small interfering RNA; NF-κB, nuclear factor kappa B; GST, glutathione S-transferase; TUNEL, terminal deoxynucleotidyl transferase dUTP nick-end labeling; LC–MS/MS, liquid chromatography–tandem mass spectrometry.

Supplementary Table 4 | Target sequences and cloning oligonucleotides for shRNA constructs.

The table lists the shRNA construct, target region, 21-nucleotide target sequence, GC content, and forward and reverse cloning oligonucleotides. All sequences are shown in the 5′ to 3′ direction. CDS, coding sequence; shRNA, short hairpin RNA; shNC, nontargeting short hairpin RNA control.

Figure 1. Integrated single-cell analyses and multidimensional screening identify RNF19A as a CRPC-associated E3 ubiquitin ligase

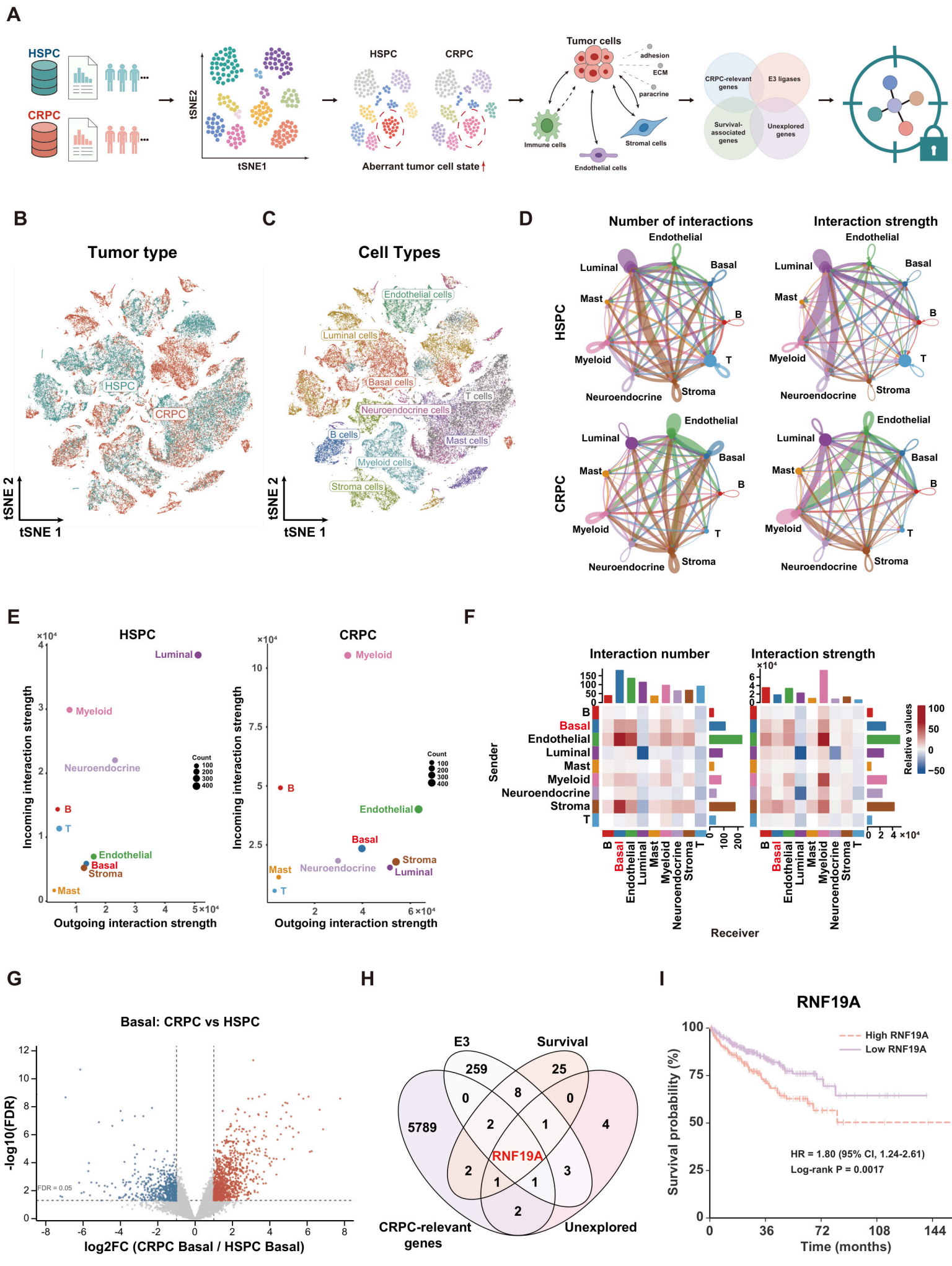


Figure 2. RNF19A supports prostate cancer cell proliferation, survival, and androgen-independent tumour growth

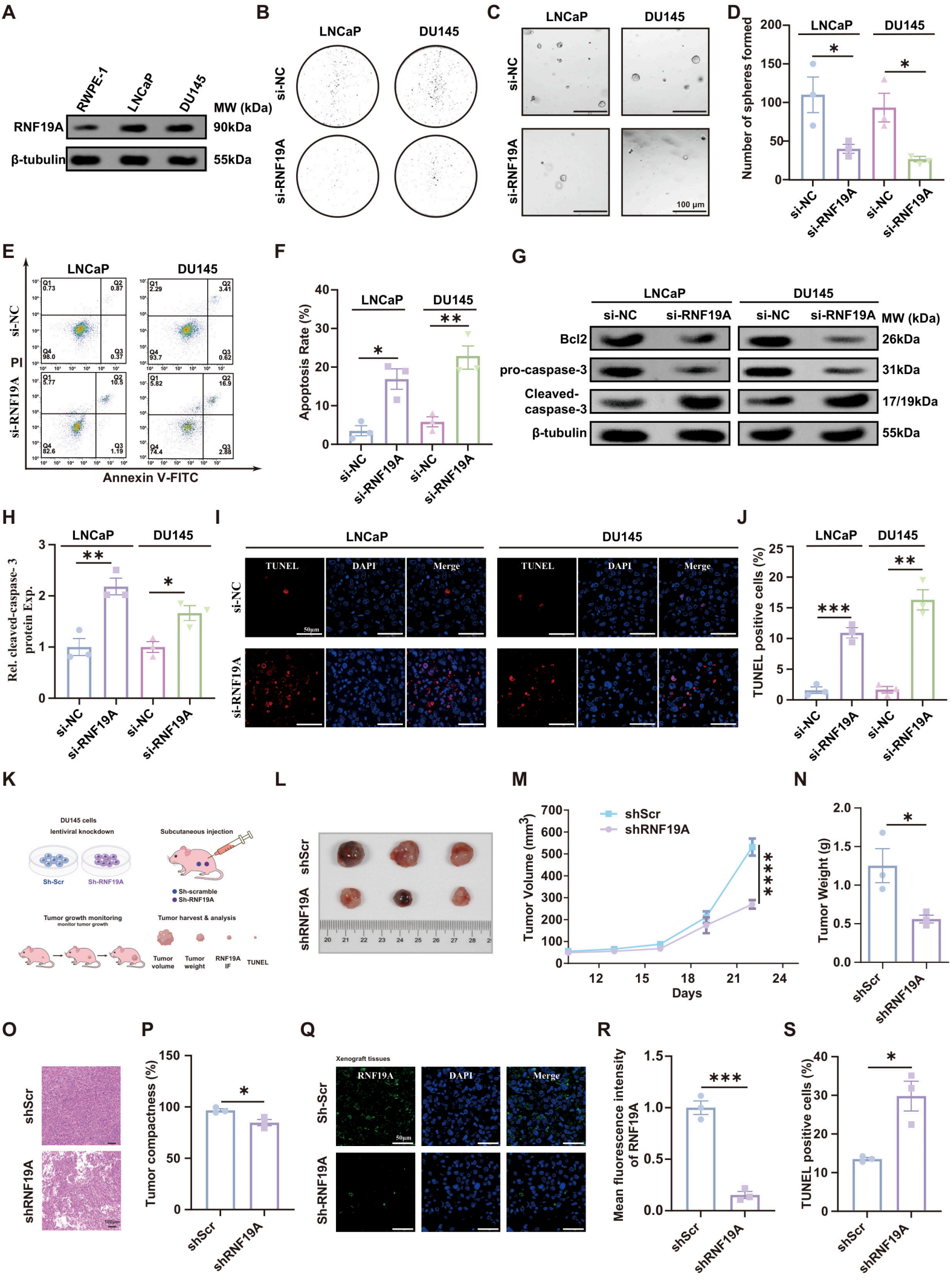


Figure 3. RNA-seq and metabolic assays reveal that RNF19A sustains energy metabolism in prostate cancer cells

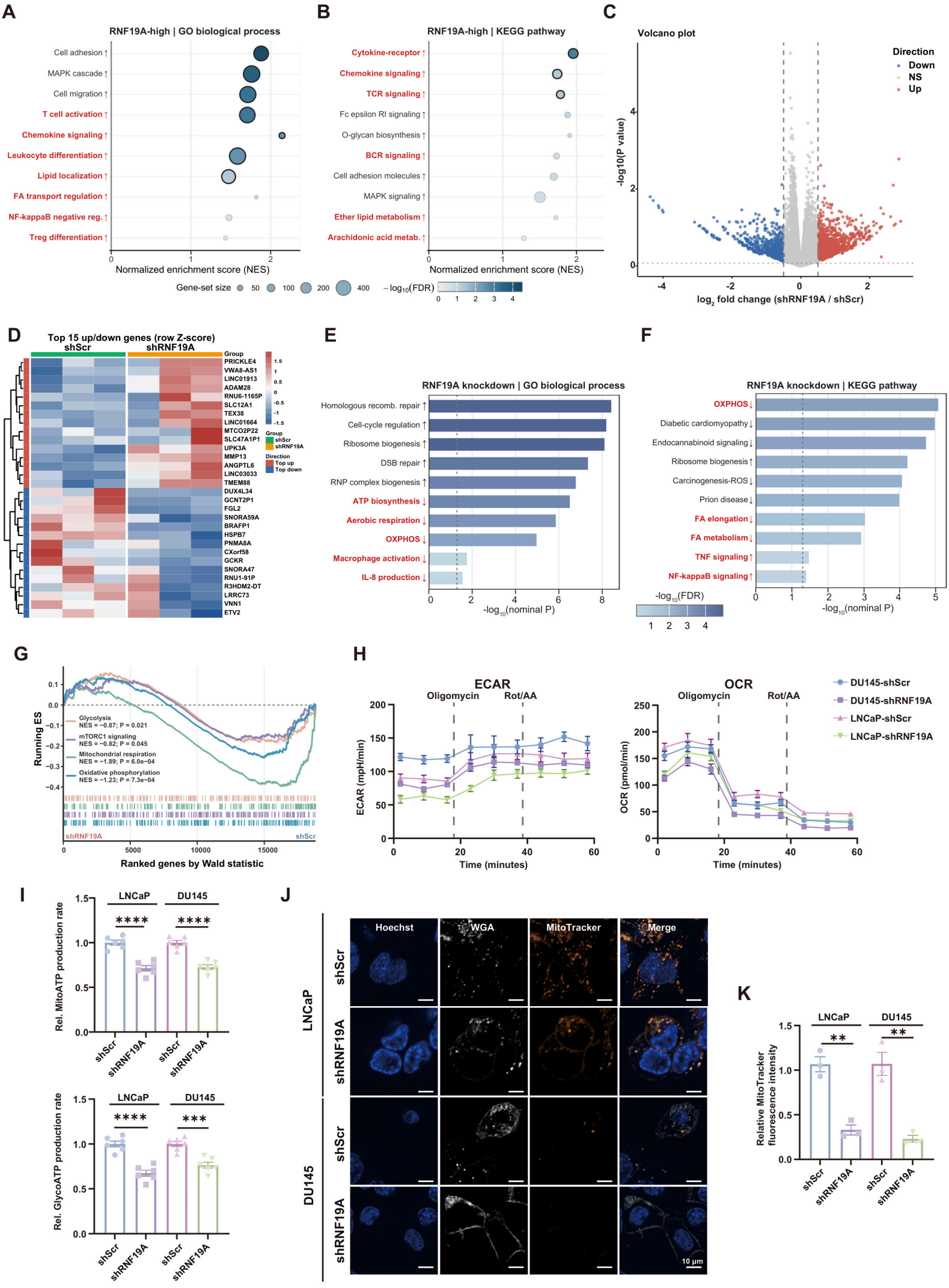


Figure 4. RNF19A interacts with p53 and promotes its ubiquitin–proteasome-dependent degradation

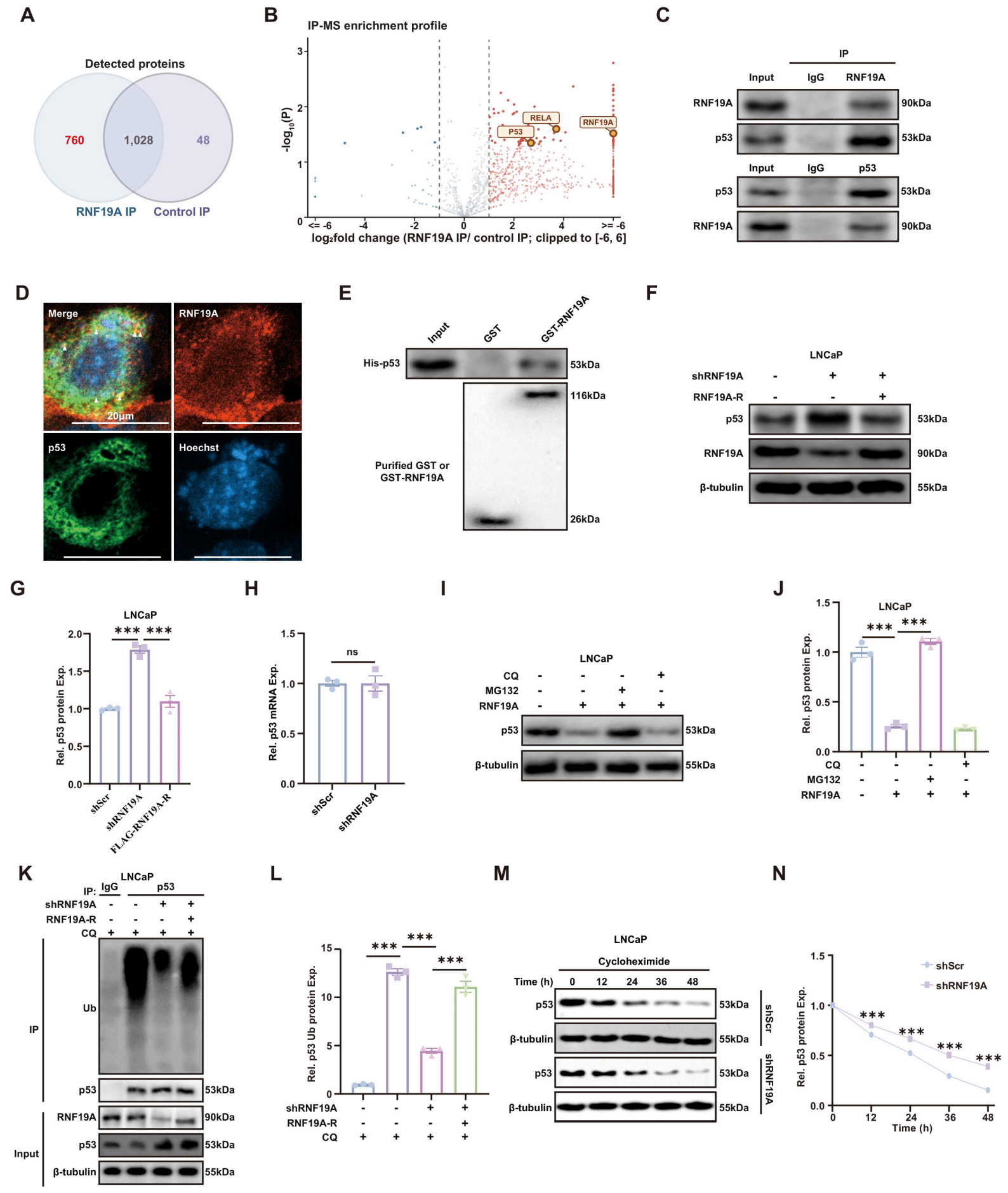


Figure 5. RNF19A-high tumour-like niches are associated with immune-suppressive microenvironment remodeling in CRPC

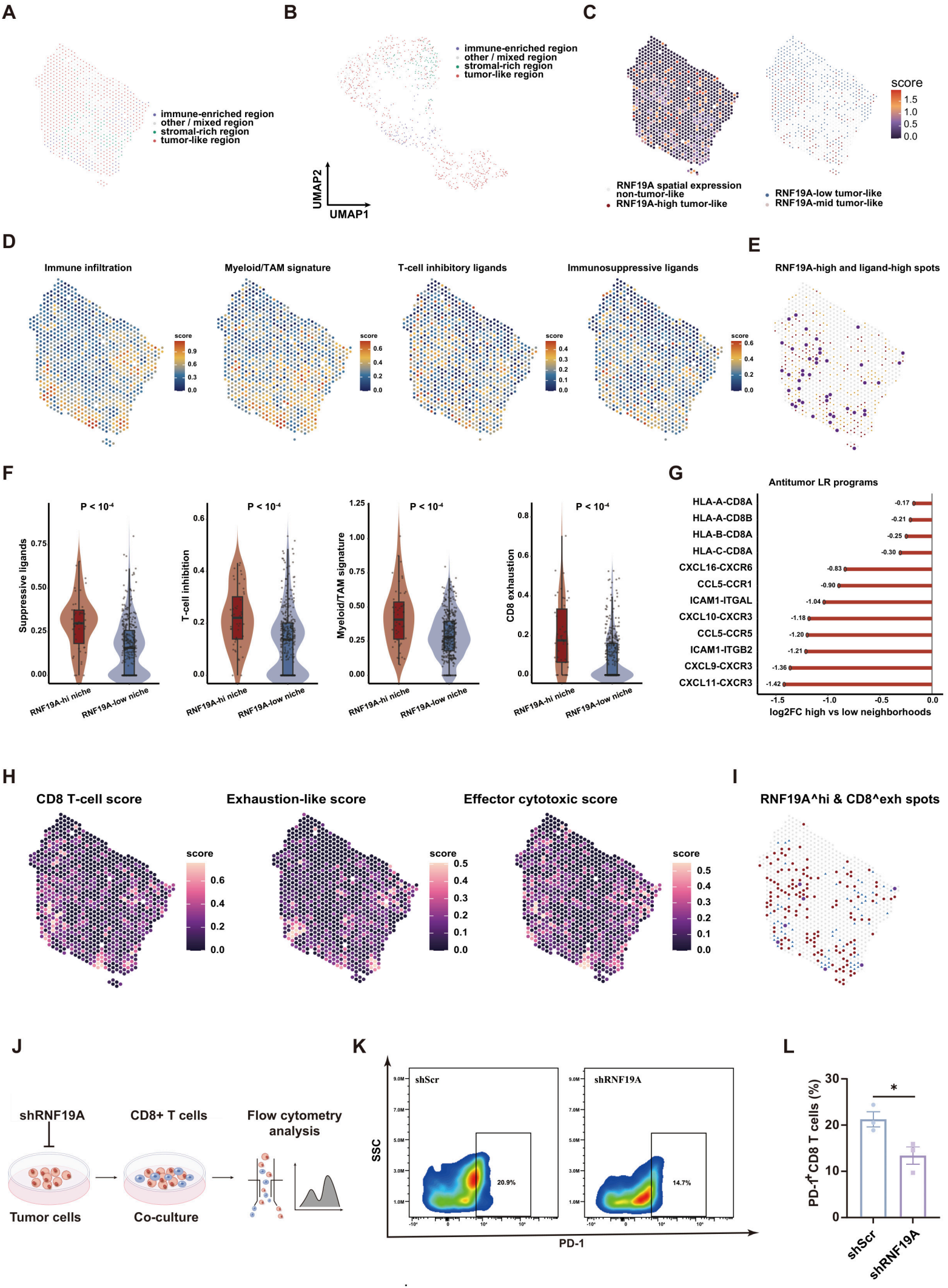


Figure 6. RNF19A promotes RELA ubiquitination and suppresses NF-κB-dependent immune activation outputs in CRPC tumour cells

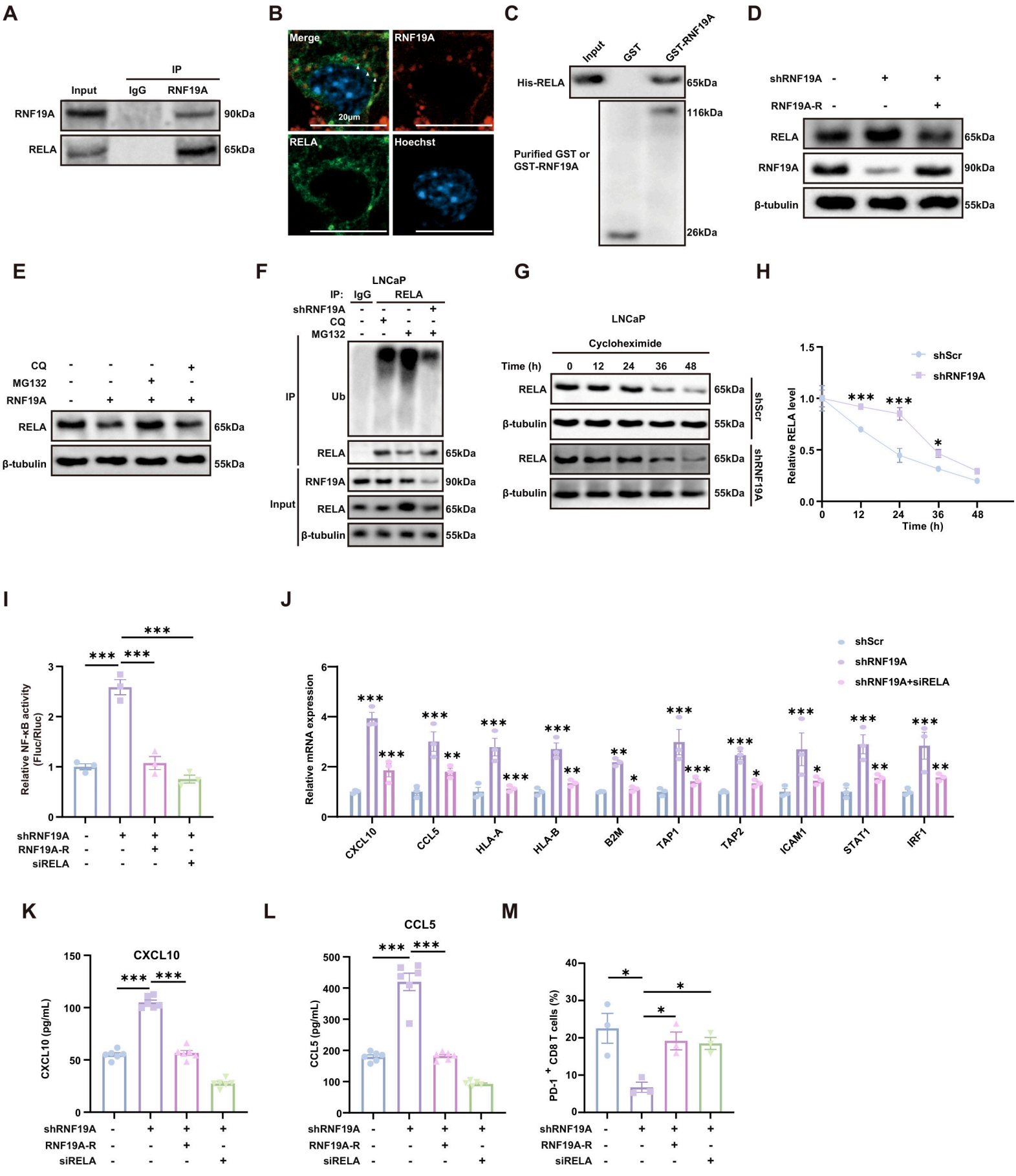
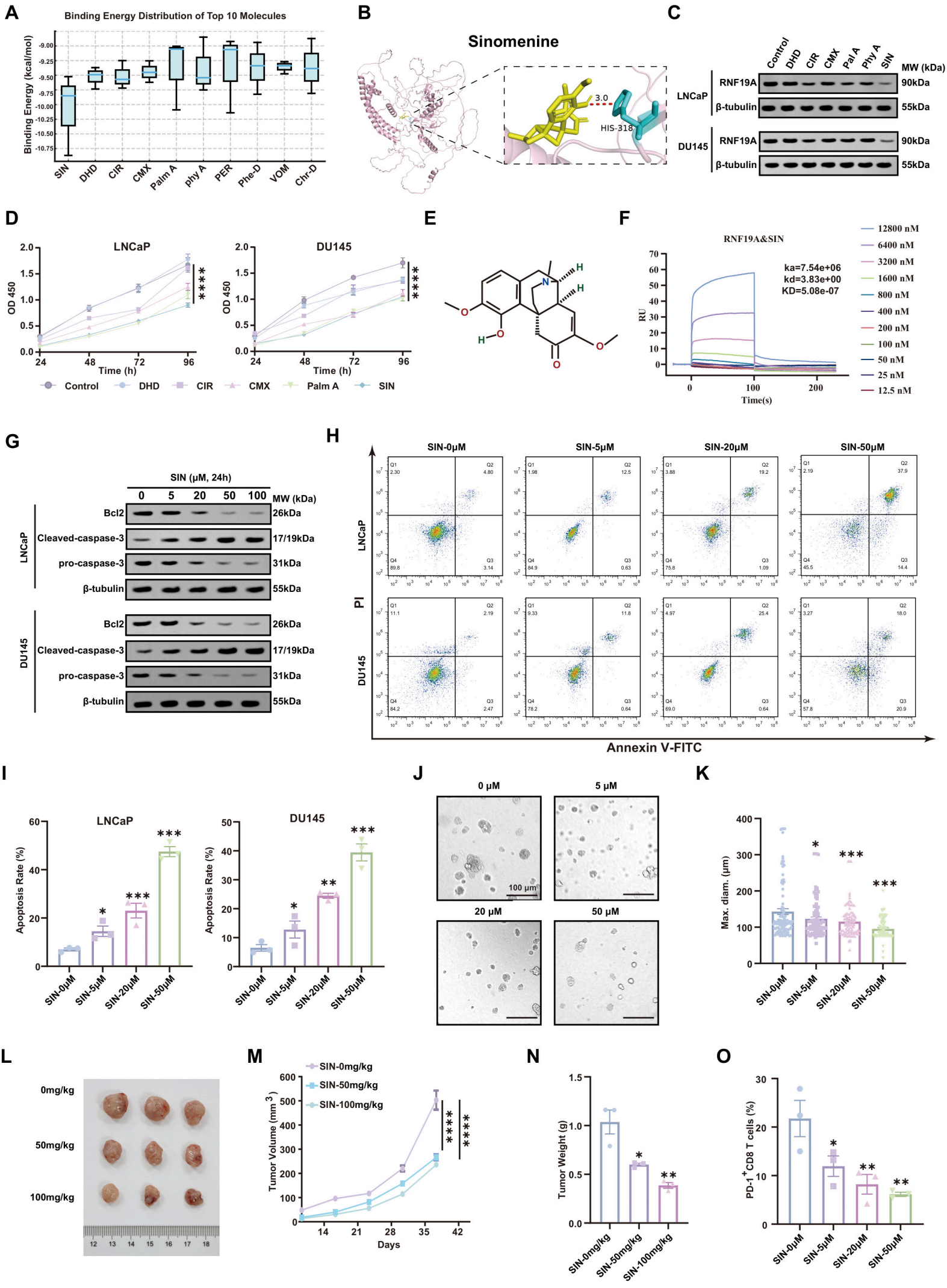
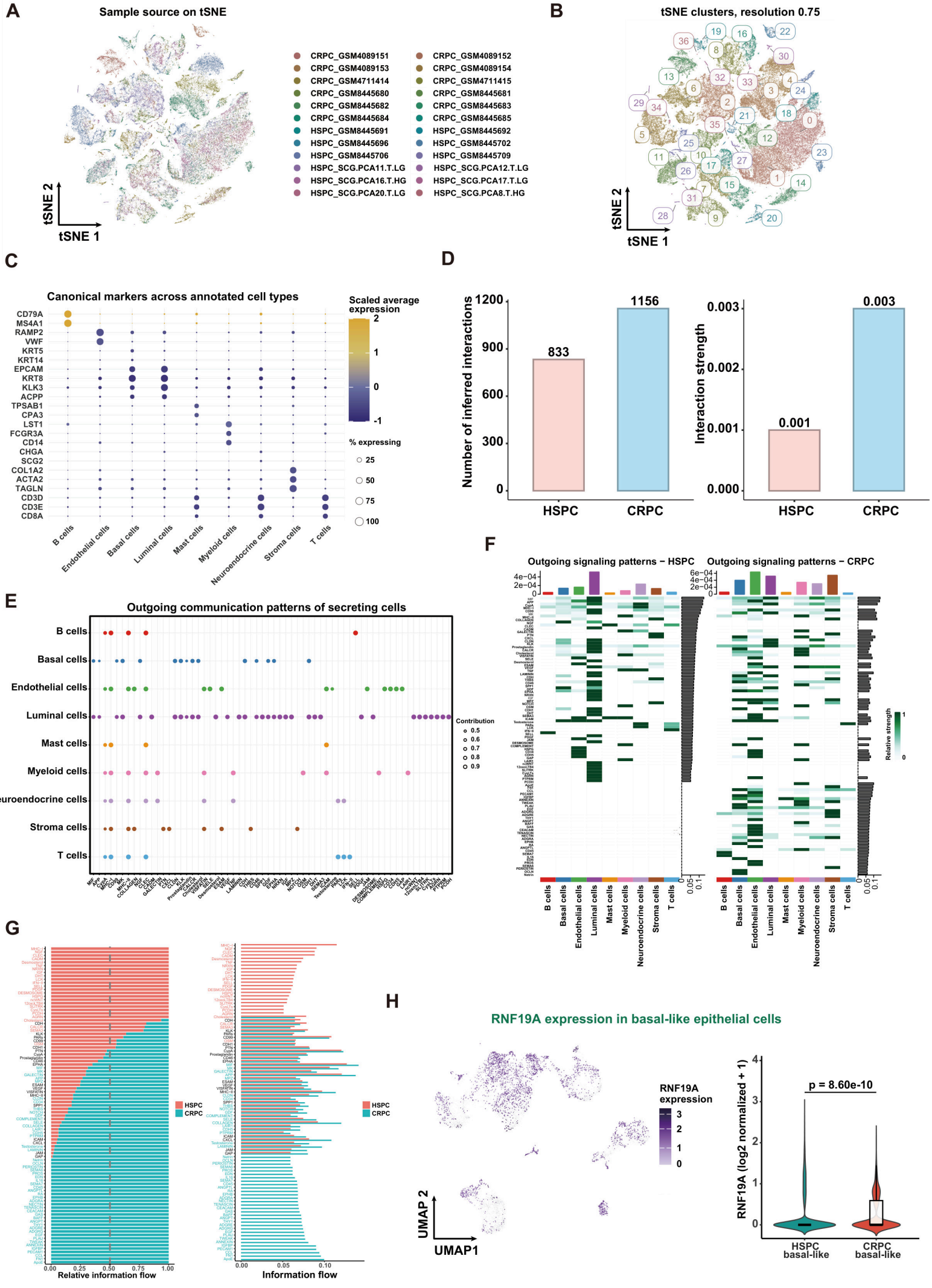


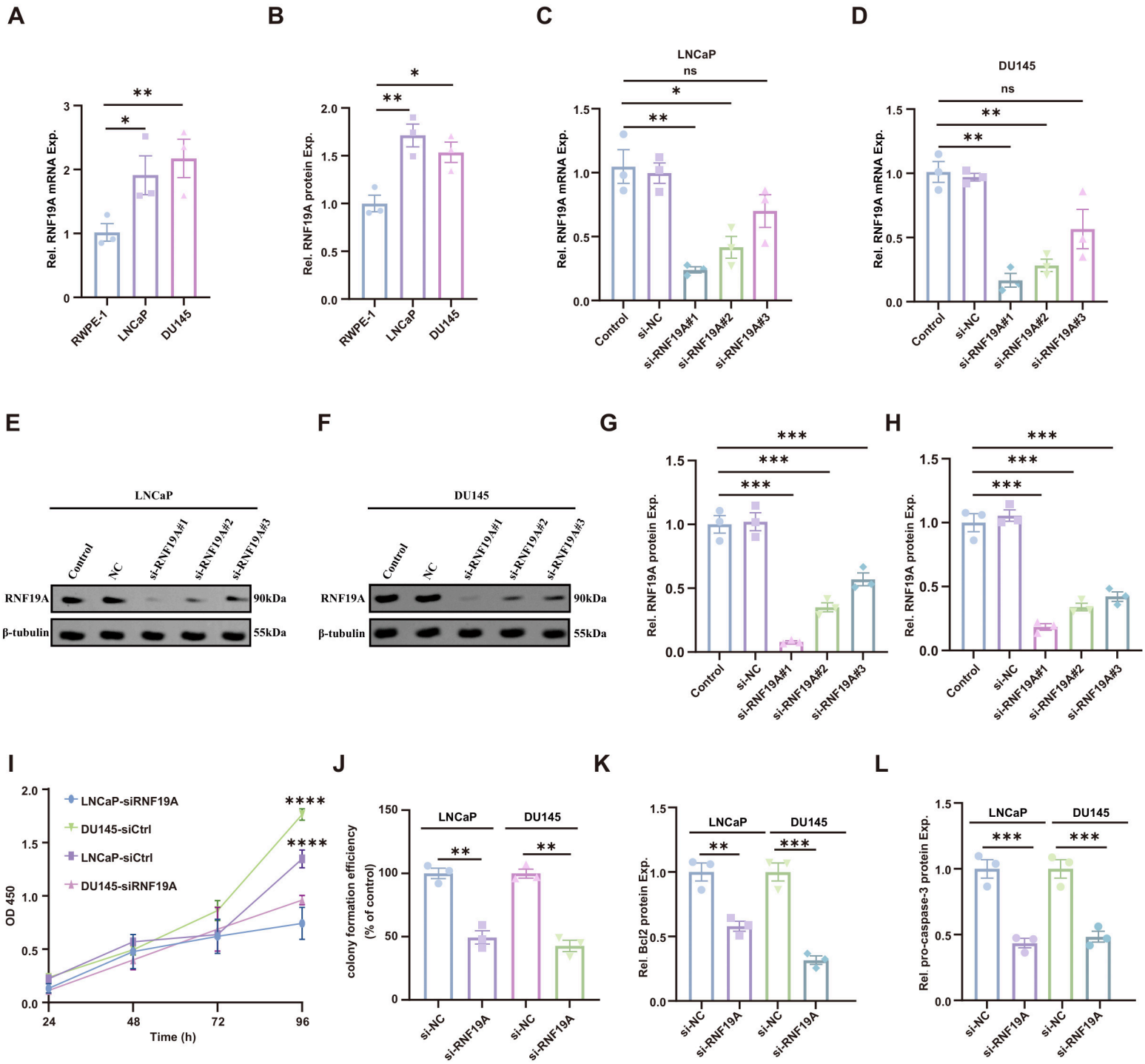
Figure 7. Sinomenine is identified as a candidate RNF19A-binding natural product and suppresses CRPC tumour growth



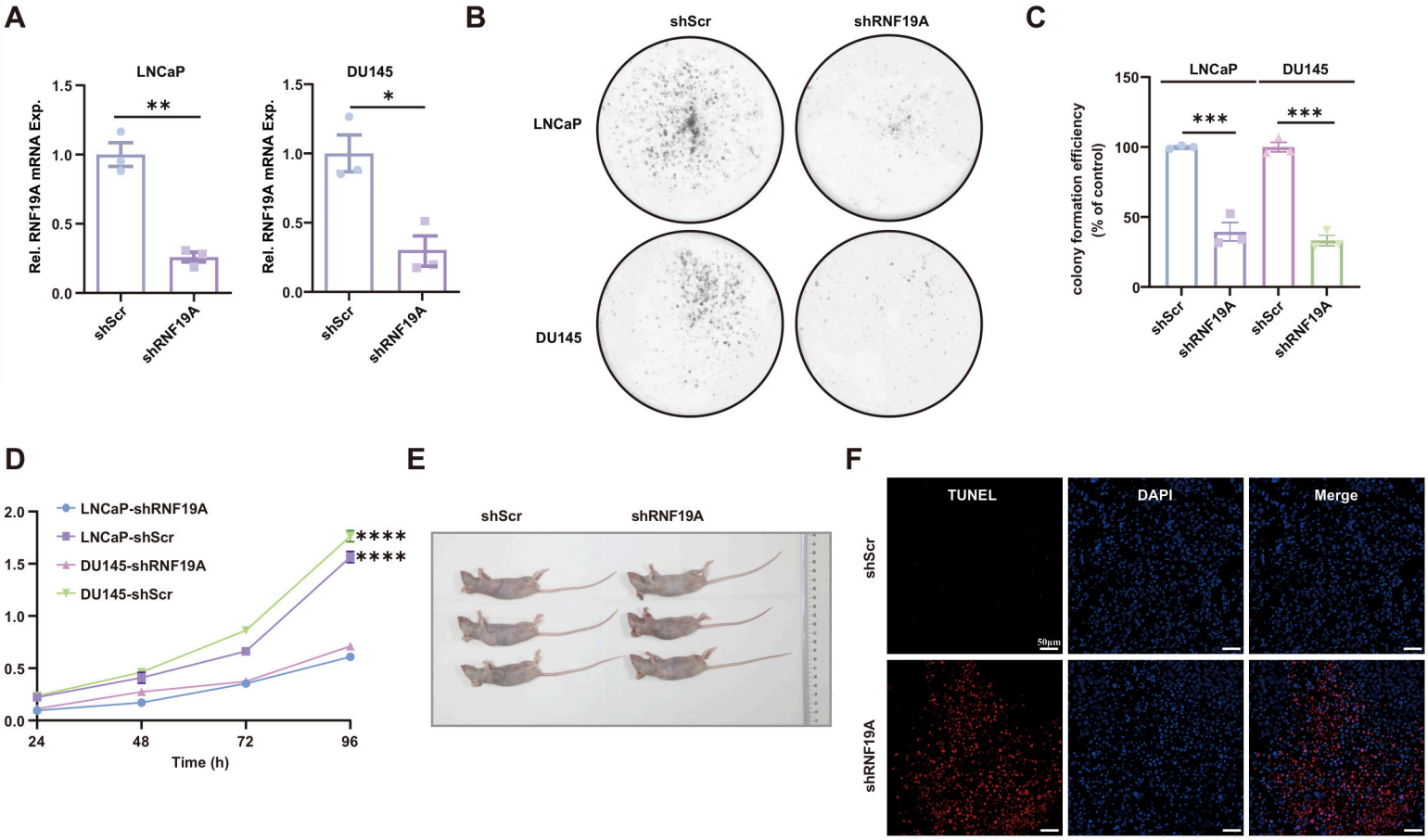
SupFig1.Integrated single-cell analysis and multidimensional screening identify RNF19A as a CRPC-associated E3 ubiquitin ligase



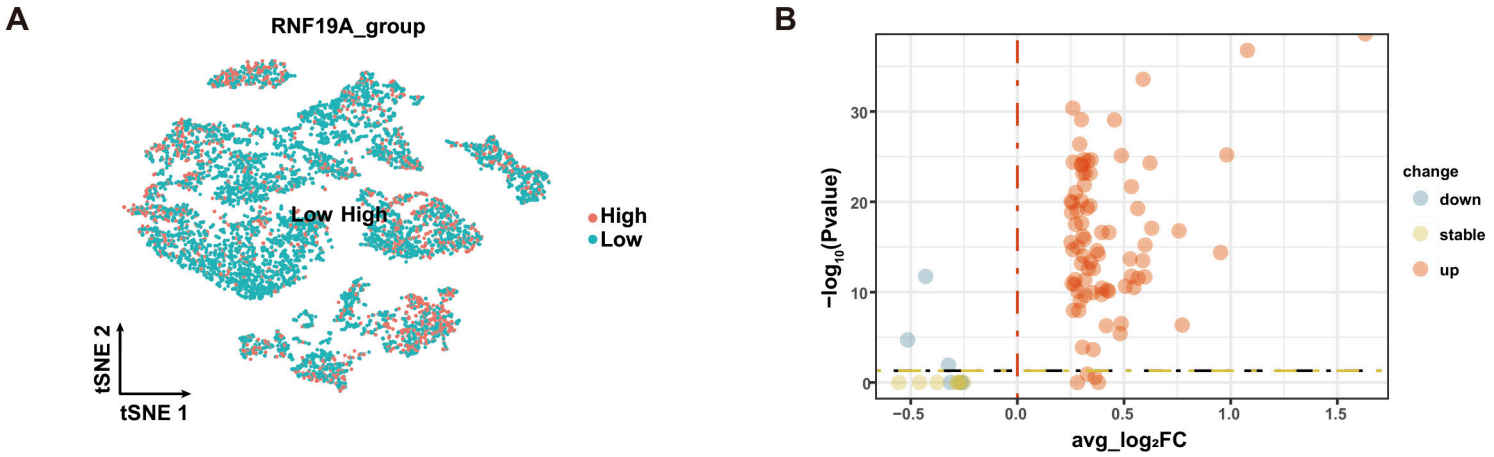
SupFig2.RNF19A is upregulated in prostate cancer cells and efficiently silenced by siRNAs



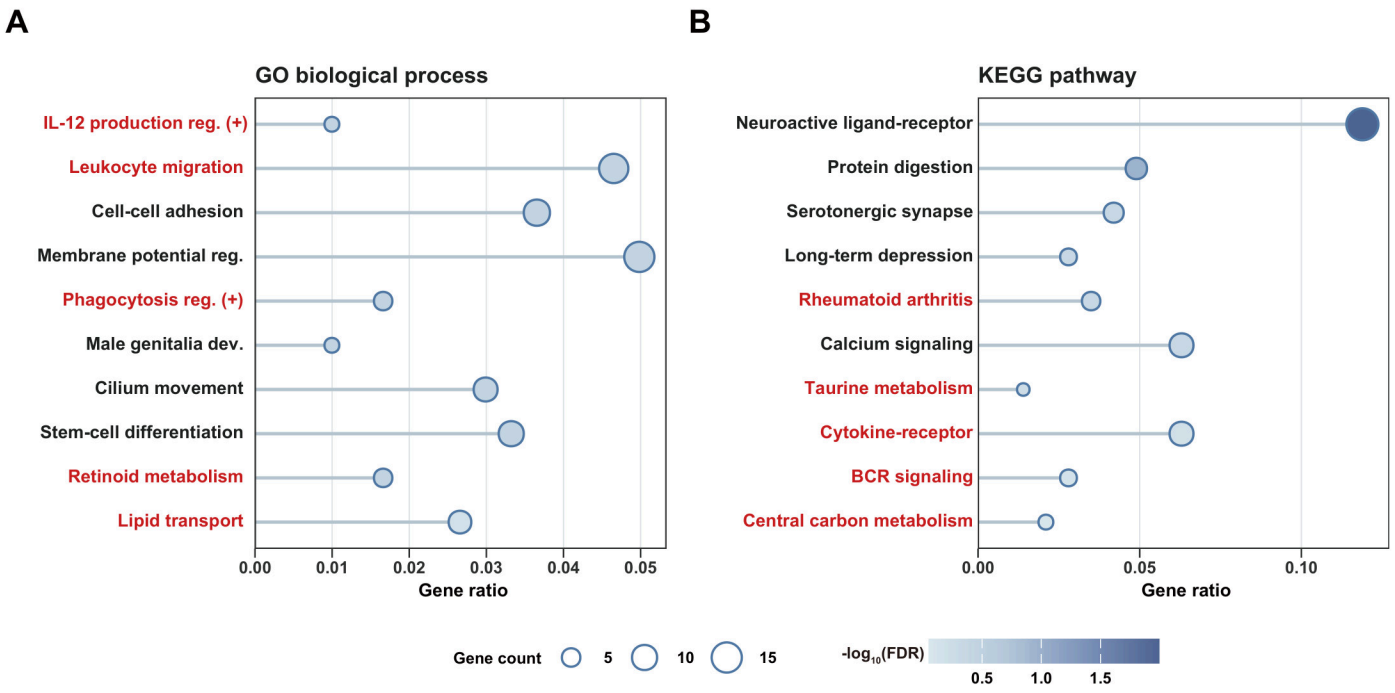
SupFig3.Stable RNF19A knockdown suppresses long-term prostate cancer cell growth and promotes apoptosis in xenograft tumours



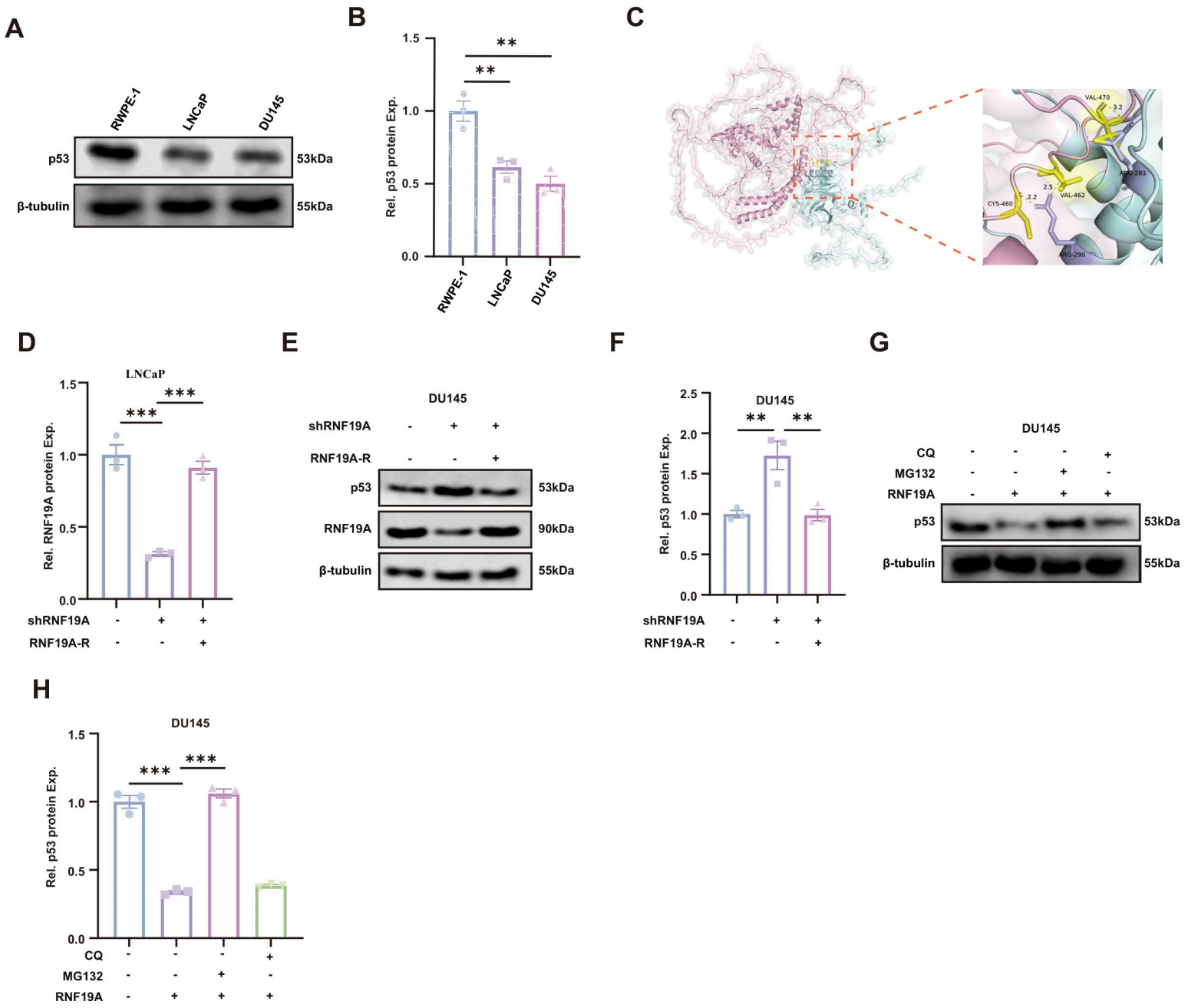
SupFig4.RNF19A-high tumour epithelial cells are associated with metabolic and immune-related programs



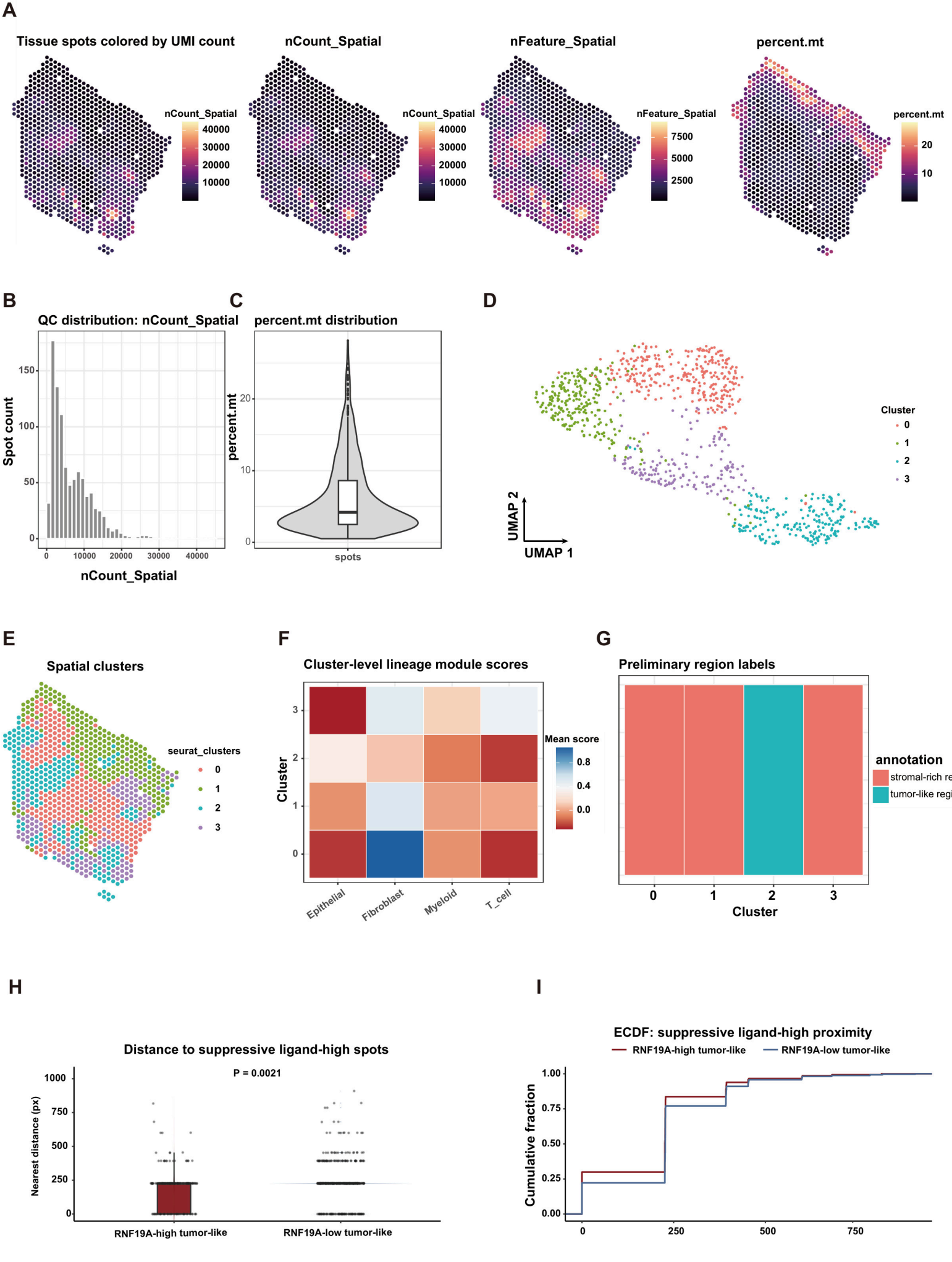
SupFig5.GO and KEGG enrichment analysis of upregulated genes after RNF19A knockdown



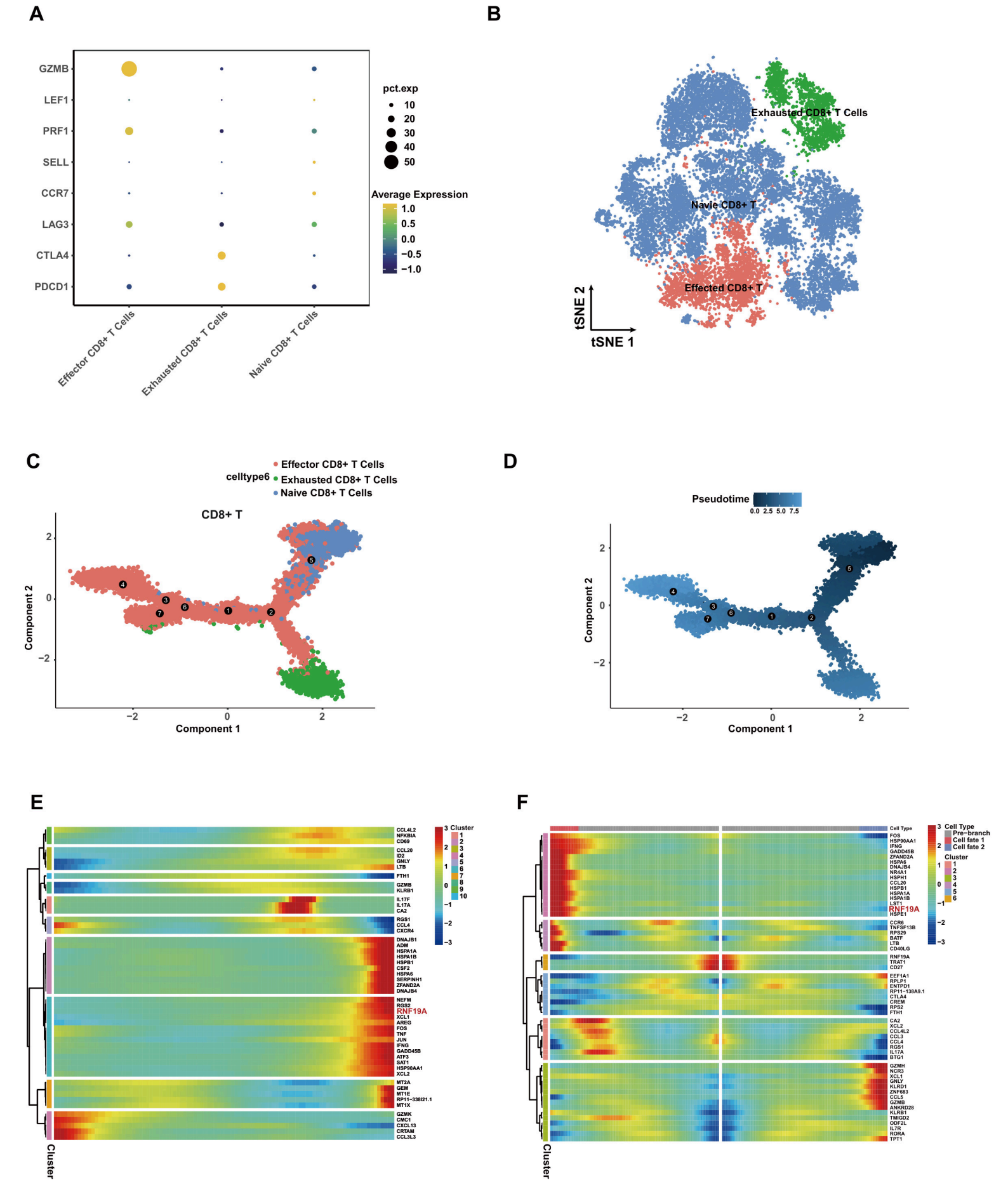
SupFig6.Supporting evidence for RNF19A-mediated regulation of p53 protein stability



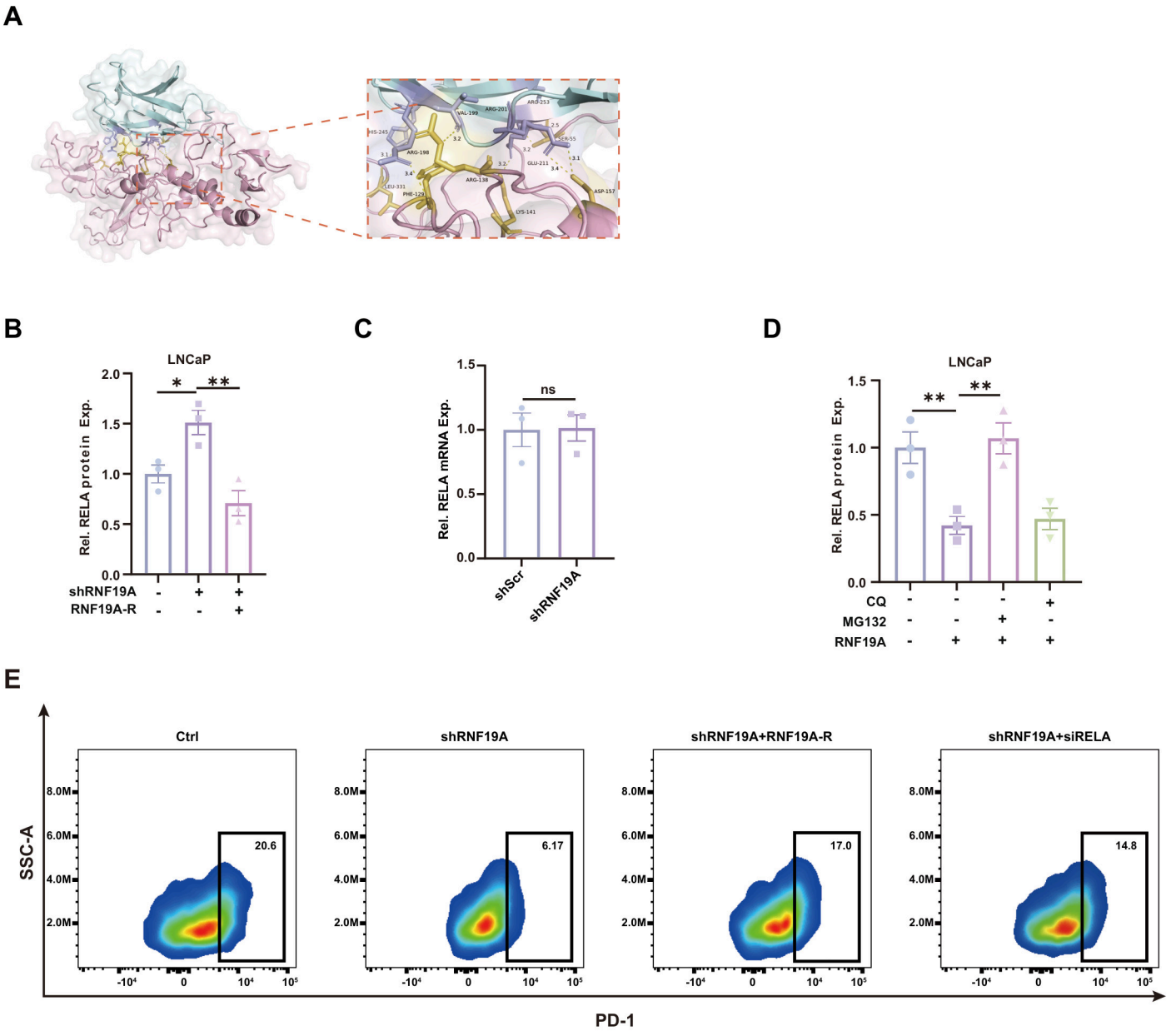
SupFig7.Spatial transcriptomic quality control and RNF19A-high tumour-like spot definition



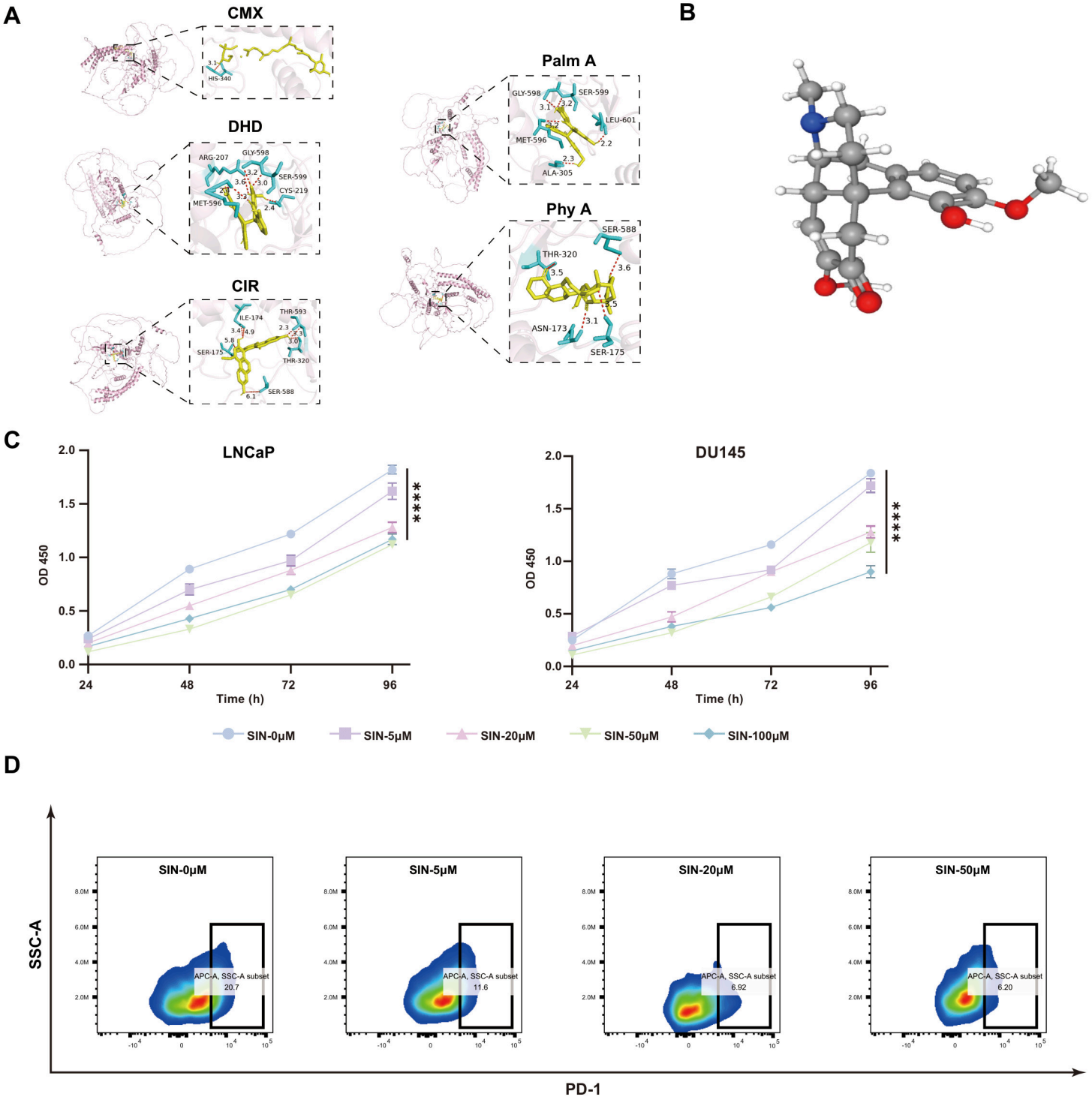
SupFig8.Single-cell trajectory analysis of CD8 T-cell exhaustion in CRPC



SupFig9.Additional validation of RNF19A-mediated RELA destabilization and RELA-dependent immune activation outputs



SupFig10.Additional validation of natural product docking, sinomenine activity, and RNF19A–RELA-dependent regulation of PD-1+ CD8 T cells



SupFig11.Schematic model of RNF19A-driven CRPC progression and sinomenine-mediated therapeutic intervention

